MASTER THESIS

DRUG-LOADED IRONSPERM CLUSTERS: MODELING, ACTUATION AND ULTRASOUND IMAGING

CONFIDENTIAL

Kaz I.N.A. Middelhoek

UNIVERSITY OF TWENTE.

Preface

Dear reader,

In front of you lies the culmination of my work over the past months. During this time, I've learnt a lot about modeling, magnetism, movement at the microscale, scientific discourse and even video editing. However, I definitely didn't do it alone. The main body of this thesis, which has been submitted for publication, wouldn't be complete without the drug loading experiments performed by Veronika Magdanz. While I performed the formation, actuation and ultrasound experiments, I wouldn't have been able to do so, without the assistance of the other (PhD) students at SRL, as they showed me how to handle the existing experimental setups and thought along with me on how to build new setups. Of course, I'd also like to thank my graduation committee: Islam, for always being available for any questions and support, for sharing his thoughts on how to shape the research, and for working with me on the manuscript; Leon, for his critical questions and inputs, that always led to a deeper understanding of the matter, and for his sharp comments on current science and education practices, which were a welcome perspective; and Sarthak, for showing his interest in my research during the SRL meetings.

Kaz Middelhoek

Enschede, 2022

Abstract

Individual biohybrid microrobots have the potential to perform biomedical *in vivo* tasks such as remote-controlled drug and cell delivery and minimally invasive surgery. This work demonstrates the formation of biohybrid sperm-templated clusters under the influence of an external magnetic field and essential functionalities for wireless actuation and drug delivery. Ferromagnetic nanoparticles are electrostatically assembled around dead sperm cells, and the resulting nanoparticle-coated cells are magnetically assembled into three-dimensional biohybrid clusters. The aim of this clustering is threefold: First, to enable rolling locomotion on a nearby solid boundary using a rotating magnetic field; second, to allow for noninvasive localization; third, to load the cells inside the cluster with drugs for targeted delivery. A magneto-hydrodynamic model captures the rotational response of the clusters in a viscous fluid, and predicts an upper bound for their step-out frequency, which is independent of their volume or aspect ratio. Below the step-out frequency, the rolling velocity of the clusters increases nonlinearly with their perimeter and actuation frequency. During rolling locomotion, the clusters are localized using ultrasound at a relatively large distance, which makes these biohybrid clusters promising for deep-tissue applications. Finally, we show that the estimated drug load scales with the number of cells in the cluster and can be retained for more than 10 hours. The aggregation of microrobots enables them to collectively roll in a predictable way in response to an external rotating magnetic field, and enhances ultrasound detectability and drug loading capacity compared to the individual microrobots. The favorable features of biohybrid microrobot clusters place emphasis on the importance of the investigation and development of collective microrobots and their potential for *in vivo* applications.

Keywords: microrobot aggregation, sperm, drug delivery, magnetic actuation, ultrasound

Contents

1. Introduction

Microrobots have the potential for numerous biomedical *in vivo* applications, such as remote-controlled drug and cell delivery [1] and minimally invasive surgery [2, 3]. The ability of these untethered microrobots to access hard-to-reach locations is promising, but multiple hurdles need to be overcome. Among these hurdles, remote actuation, non-invasive localization, and biocompatibility are some of the most challenging from an implementation perspective, as they have to be addressed simultaneously and their trade-offs must be quantified [3, 4]. The small scale of microrobots limits the use of built-in power sources and actuators. Therefore, various external power sources on the microscale have been proposed, such as magnetic fields [5–7], optical energy [8, 9], ultrasound waves [10, 11], chemical reactions [12, 13], and combinations of some of these stimuli [14]. Magnetic fields are particularly promising for *in vivo* settings, as they allow for remote, long-range and biocompatible actuation. The magnetic field and gradient can exert sufficient force and torque on microrobots, enabling six-degrees-of-freedom motion [5, 6, 15–22]. In order to not only actuate, but also localize and track the motion of the microrobot in an *in vivo* setting, the magnetic actuation needs to be combined with an imaging modality [23–25]. For the localization of microrobots, existing medical imaging modalities such as photoacoustic computed tomography [26], positron emission tomography [27], magnetic resonance imaging [28], photoacoustic imaging [29], and ultrasound [30] have been explored. Each of these medical imaging modalities has different requirements, such as sufficient contrast agents, echogenicity or the presence of radioactive agents. Among these techniques, ultrasound imaging is a potential option for noninvasive localization and has been established as a standard clinical diagnostic tool. It is radiation-free and provides real-time imaging, allowing for microrobot tracking [31–34]. For *in vivo* applications, the microrobots should be biocompatible. Materials with a high level of biodegradability are the ideal choice, because they do not have to be retrieved after use, nor do they accumulate in organs and trigger chronic inflammatory responses [35]. Biohybrid microrobots, which consist of biological and synthetic components, offer this functionality. The biohybrid integration provides additional advantages, such as adaptability to physiological environment, facile cargo loading, and efficient motion on the microscale [36].

Recently, biohybrid microrobots based on bacteria [28, 37–39], algae [40], cardiomyocytes [41], and sperm cells [42–44] have been developed to offer enhanced biocompatibility and motion under physiological conditions. For example, spermatozoa have been explored as templates for flexible magnetically actuated microrobots [45] due to their intrinsic flexibility and drug loading capacity. Coating the flexible body of sperm cells with magnetic particles enables magnetic actuation, and at the same time increases the echogenicity of the cells to allow for ultrasound imaging [45]. Furthermore, loading the biotemplated microrobots with anticancer drugs has also been demonstrated, which is an essential step in producing microrobots with some basic functionalities.

For practical biohybrid microrobots systems it is necessary to achieve further improvements in terms of locomotion efficiency, localization, and drug loading capability, before they can be used for targeted drug delivery. The locomotion velocity of individual microrobots is limited by the their maximum generated propulsive thrust. The individual microrobots can hardly be localized *in vivo* due to the spatial resolution and contrast-to-noise ratio of existing medical imaging modalities. Additionally,
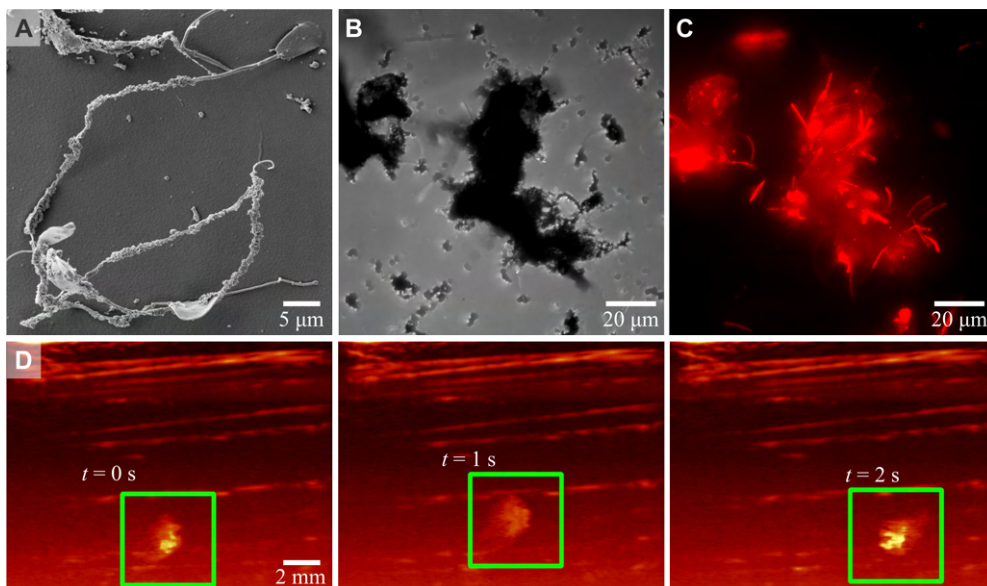
Figure 1. Biohybrid IRONSperm clusters consist of dead bovine sperm cells, coated with iron nanoparticles. **(A)** Scanning electron micrograph of several entangled IRONSperm, the fundamental building blocks of the clusters. **(B)** Bright-field image of an IRONSperm cluster. **(C)** Fluorescent image of Doxorubicin hydrochloride (DOX-HCl)-loaded IRONSperm cluster. The cancer drug DOX-HCl, which has been taken up by the sperm cells, emits a fluorescent signal and thereby makes the sperm cells visible. **(D)** Due to their nanoparticle coating, IRONSperm clusters reflect detectable ultrasound waves. In the ultrasound images, the cluster (green square) is pulled by a magnetic field gradient.

due to its volume, a single microrobot can carry a limited amount of drugs. To achieve a relevant therapeutic outcome by the action of microrobots, research should move toward a greater degree of collaborative and collective behavior of the robots. Combining several magnetic microrobots into a cluster results in a larger amount of magnetic material and thus increases the magnetic moment of the microrobots, so that a greater magnetic torque can be exerted compared to a single microrobot. Self assembly of microrobots also introduces new forms of actuation, such as rolling on a surface when they form a three-dimensional geometry [46]. Further, a greater detectable signal for noninvasive localization can be produced, and a greater volume of drug can be loaded and transported.

Concerted robot action is not only important in biohybrid robotic implementation but is inspired by processes in nature. Collective behavior of individual organisms or cells has been observed in many biological systems, such as the flocking of birds, schooling of fish, swarming of bacteria, and clustering of worms [47, 48]. Sperm cells, in particular, show collective behavior to adapt to their surroundings [49]. Simple microrobots in the shape of spheres [50, 51] or disks [52] have been magnetically actuated to show collective behavior and to merge, split, and reshape. Liquid metal rods have been acoustically actuated to provide a similar response to those of the spheres and disks [53]. Microrobot swarms can follow trajectories [54], collaborate in potential additive manufacturing applications [55], transport cargo [56], and are
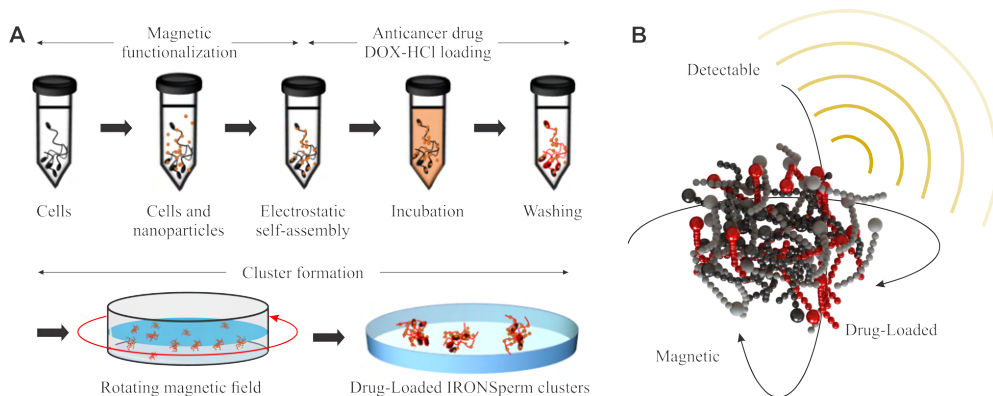
Figure 2. Biohybrid IRONSperm clusters are produced and magnetically functionalized for wireless actuation, noninvasive localization, and drug loading. **(A)** Nanoparticles are electrostatically assembled around bovine sperm cells. The resulting microrobots are loaded with doxorubicin-HCl (DOX-HCl), and magnetically attracted to form IRONSperm clusters, using a rotating magnetic field. **(B)** IRONSperm clusters can reflect a detectable ultrasound wave, align with an external magnetic field, and carry drug cargo.

functional in bio-fluids [57]. Besides synthetic microrobots, swarms of magnetotactic bacteria have been steered through vascular structures [58] and used in micro-assembly tasks [28]. These studies show that microrobot clusters improve on the capabilities of individual microrobots.

This study aims to combine the distinct advantages of biohybrid microrobots with those of collective behavior, to address several practical hurdles for microrobots in targeted drug delivery applications. Therefore, we investigate the collective behavior of nanoparticle-coated sperm cells [45, 59], which we refer to as IRONSperm (figure 1A), under the influence of a rotating magnetic field. Theoretical magneto-hydrodynamic models are developed to understand IRONSperm clustering and cluster motion in a viscous fluid. Clusters of the biohybrid microrobots (figure 1B) are formed through electrostatic and magnetic self-assembly and entanglement. These clusters are actuated to study their rotational dynamics and rolling locomotion under the influence of rotating magnetic fields. Finally, drug loading of the IRONSperm clusters with doxorubicin-HCl (figure 1C) is investigated, and noninvasive localization using ultrasound imaging is demonstrated (figure 1D, video S1 in supplementary material). While the ultrasound localization of IRONSperm clusters has been demonstrated before [45], this study improves the localization in multiple ways. First, ultrasound localization is shown during magnetic actuation, instead of while moving by fluid convection. Second, the clusters are localized at a significantly larger distance and using a lower ultrasound wave frequency.

2. Cluster Formation by Electrostatic Self-Assembly and Magnetic Attraction

A suspension of dead bovine sperm cells and iron nanoparticles self-assembles into IRONSperm, due to the electrostatic forces between the negatively charged sperm cell membranes and the positively charged nanoparticles (figure 2A) [60]. Some
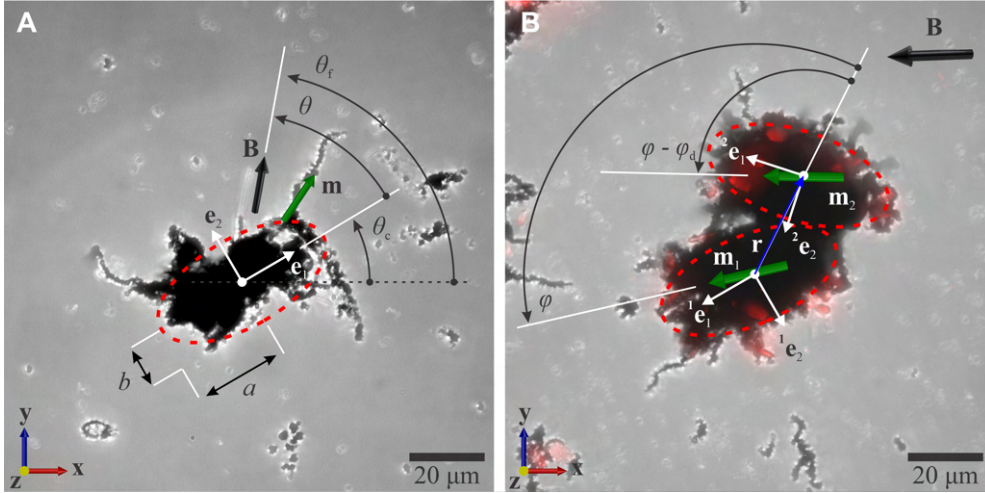
Figure 3. Clusters are approximated as ellipsoids. **(A)** An external magnetic field, **B**, magnetizes the cluster to a magnetization **m**, depending on the demagnetizing factors of the cluster. **(B)** Two clusters separated by **r** aggregate in a rotating magnetic field, leading to the formation of a larger cluster. The remanence magnetization and entanglement enables the two clusters to remain attached when the magnetic field is removed.

IRONSperm entangle due to physical interactions, forming clusters (figure 2B). These clusters and individual IRONSperm are further aggregated using an external magnetic field. In a magnetic field **B**, the soft-magnetic IRONSperm clusters are magnetized to a magnetic moment **m** (figure 3A). At low field strengths, the magnetic moment increases linearly with the field strength (section 9.2 and figure S2 in supplementary material). The coercivity of the clusters is 41 mT. The direction of a cluster's magnetic moment is dependent on the magnetic field direction θ_f, the cluster orientation θ_c, the demagnetizing factor n_a in the preferred magnetization direction of the cluster $\mathbf{e}_1$, and the demagnetizing factor n_r in the direction $\mathbf{e}_2$, perpendicular to $\mathbf{e}_1$, as shown in figure 3A.

When applying a uniform magnetic field in a low Reynolds number environment far from any solid boundary, the translational motion of a magnetized IRONSperm cluster is governed by the viscous drag force, $\mathbf{F}_d$, and the magnetic force, $\mathbf{F}_m$, exerted by surrounding clusters, such that $\mathbf{F}_d + \mathbf{F}_m = 0$. The viscous drag force is given by $\mathbf{F}_d = -f_t\mathbf{v}$, where f_t is the translational drag coefficient of the cluster and $\mathbf{v}$ is its velocity. The magnetic force that a cluster with magnetic moment $\mathbf{m}_1$ exerts on a neighboring cluster with a magnetic moment $\mathbf{m}_2$ is given by [61]

$$\mathbf{F}_m = \frac{3\mu_0}{4\pi|\mathbf{r}|^4}\left(\mathbf{m}_2\left(\mathbf{m}_1\cdot\hat{\mathbf{r}}\right) + \mathbf{m}_1\left(\mathbf{m}_2\cdot\hat{\mathbf{r}}\right) + \hat{\mathbf{r}}\left(\mathbf{m}_1\cdot\mathbf{m}_2\right) - 5\hat{\mathbf{r}}\left(\mathbf{m}_1\cdot\hat{\mathbf{r}}\right)\left(\mathbf{m}_2\cdot\hat{\mathbf{r}}\right)\right), \quad (1)$$

where $\hat{\mathbf{r}}$ is the unit vector between the clusters and $|\mathbf{r}|$ is the distance between the clusters (figure 3B). Note that the force decreases with the fourth power of the distance between the clusters ($|\mathbf{F}_m| \sim |\mathbf{r}|^{-4}$). This means that the time for neighboring clusters to reach each other scales with the fifth power of the distance between them [62]. Magnetic attraction is therefore only suited for relatively short distances and makes the resulting cluster shape and size dependent on the concentration of the nanoparticles and nanoparticle-coated sperm cells in the suspension.

When the magnetic field is allowed to rotate, the clusters trail behind the field, as they try to align their preferred magnetization axis with the field. When two neighboring clusters rotate in sync with an external magnetic field, the average attractive force between them per field rotation is given by

$$\frac{1}{2\pi}\int\limits_0^{2\pi} \mathbf{F}_m \cdot (-\hat{\mathbf{r}}) \mathrm{d}\varphi = \frac{3\mu_0 |\mathbf{m}_1||\mathbf{m}_2|}{8\pi |\mathbf{r}|^4} \cos(\varphi_d), \tag{2}$$

where φ is the angle between $\mathbf{r}$ and $\mathbf{m}_1$, and φ_d is the angle between $\mathbf{m}_1$ and $\mathbf{m}_2$, such that $-\pi/2 \le \varphi_d \le \pi/2$. This force is positive for all possible values of φ_d, causing the clusters to aggregate. A rotating magnetic field is used to form clusters. Further aggregation of these clusters in a rotating magnetic field is likely to yield ellipsoidal structures (video S3 in supplementary material). The attractive magnetic force between neighboring clusters is only noticeable at distances less than a few times their sizes, as expected based on (2). Clusters come in contact (figure 3B) and preserve a stable configuration even when the external magnetic field is removed, due to their remanence magnetization and entanglement. Therefore, the clusters may be regarded as connected rigid structures. During fast rotations, the clusters can deform or even break down into smaller bodies.

3. Characterization of the Step-Out Frequency

A magnetic field exerts a torque on an IRONSperm cluster $\boldsymbol{\tau}_m = \mathbf{m} \times \mathbf{B}$. Similarly to the force balance, in a low Reynolds number environment the magnetic torque is balanced by the viscous drag torque $\boldsymbol{\tau}_d = f_r \boldsymbol{\omega}_c$, where f_r is the rotational drag coefficient of the cluster and $\boldsymbol{\omega}_c$ is its angular velocity, such that $\boldsymbol{\tau}_m + \boldsymbol{\tau}_d = 0$. Clusters rotate to align their magnetic moment, often in the direction of their longest axis, with the magnetic field. In a uniform rotating magnetic field, the rotational movement of magnetic dipoles is given by the following differential equation:

$$\omega_c = \frac{\mathrm{d}\theta_c}{\mathrm{d}t} = \begin{cases} \omega_{so} \sin(\omega_f t - \theta_c), & \text{permanent magnet,} \quad (3a) \\ \omega_{so} \sin(2(\omega_f t - \theta_c)), & \text{soft magnet,} \quad (3b) \end{cases}$$

where ω_{so} (rad/s) is the step-out frequency, ω_f is the angular velocity of the magnetic field, and t is time. The step-out frequency is the maximum angular velocity at which a cluster rotates in synchrony with the external field, and differs for each cluster based on its magnetic moment and viscous drag coefficient. Figure 4A shows the response of a cluster under the influence of a rotating magnetic field (black arrow) at a frequency of 0.5 Hz. The external magnetic field magnetizes this cluster to magnetization $\mathbf{m}$, which allows for rotation in synchrony with the field (video S4 in supplementary material). There is a constant phase angle between the magnetic field and the cluster, which is captured by the permanent magnet model. When actuated above their step-out frequency, clusters undergo oscillations superimposed on the rotational motion (figure 4B, video S4 in supplementary material), as the cluster can no longer rotate in synchrony with the field rotations. Figure 4B shows that these oscillations are captured by the permanent magnet model, as the clusters are actuated below their coercivity field strength.

Below the step-out frequency, the phase angle θ, i.e., the angle between the preferred magnetization direction of an object and the magnetic field during field
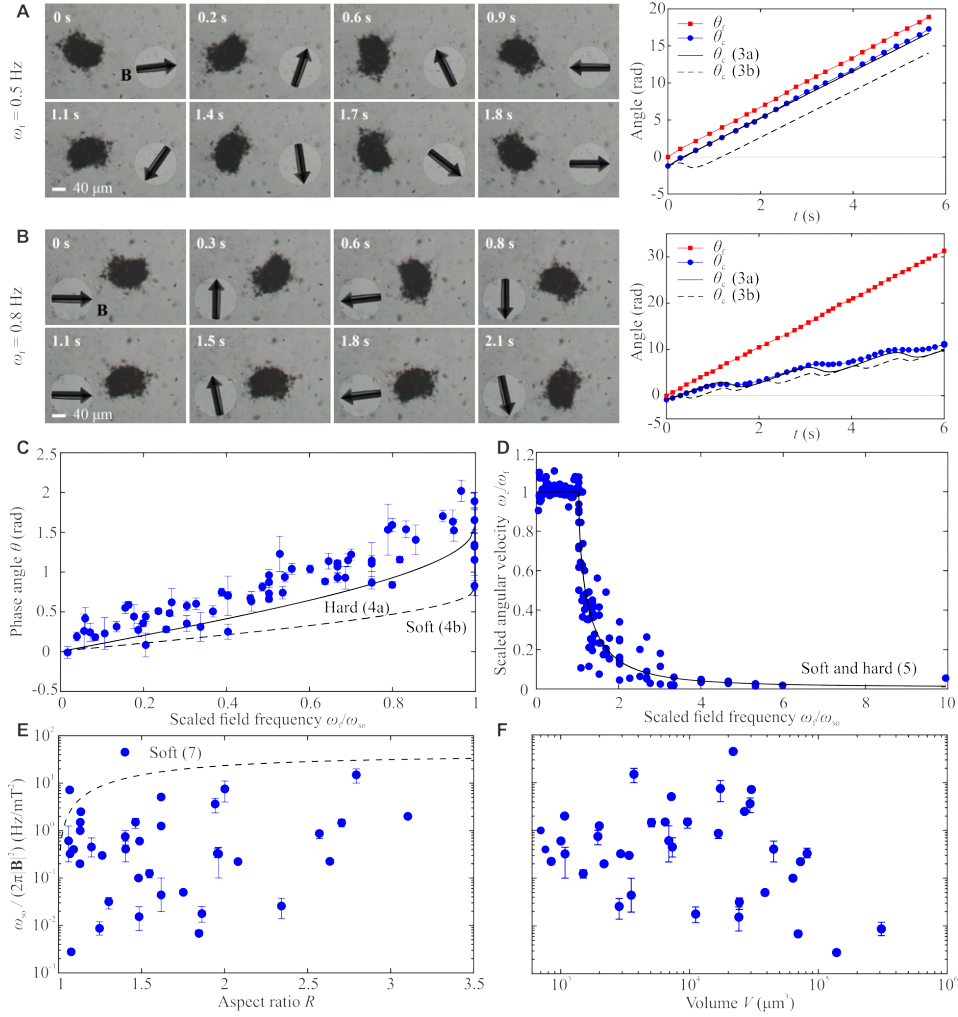
Figure 4. Motion characteristics of IRONSperm clusters. **(A)** A cluster is actuated below ω_{so} to follow an external magnetic field of 8 mT (black arrow) rotating at 0.5 Hz with a constant phase angle between the field and $\mathbf{e}_1$. The permanent magnet model resembles this cluster movement (right). θ_{f} is the field direction and θ_{c} is the cluster direction. **(B)** A cluster actuated above ω_{so} oscillates under the influence of a rotating field at 0.8 Hz. The phase angle between the field and the cluster orientation is not constant. The permanent magnet model resembles the cluster movement (right). θ_{f} is the field direction and θ_{c} is the cluster direction. **(C)** The phase angle θ between the field and $\mathbf{e}_1$ of the clusters increases with ω_{f} and is larger than the angle predicted by the soft and hard (permanent) magnet models. The error bars indicate the standard deviation of the phase angle over multiple field rotations ($n = 18$). **(D)** The average angular velocity of clusters ($n = 27$) is equal to the field angular velocity ω_{f} up to ω_{so}. Above ω_{so}, the average angular velocity of a cluster decreases with ω_{f}, in agreement with the soft and hard magnet models. **(E)** The scaled step-out frequency $\omega_{\mathrm{so}}/|\mathbf{B}|^2$ of the clusters shows no relation to the aspect ratio R of the clusters ($n = 38$). Each dot represents the mean scaled step-out frequency of a cluster. If error bars are drawn, these indicate the range of scaled step-out frequencies measured at different field strengths. The step-out frequency predicted by the soft magnet model is larger than 95% of the measurements. **(F)** The scaled step-out frequency is independent of the estimated volume of the clusters, which is in agreement with the soft and hard magnetic model. Each dot represents the mean scaled step-out frequency of a cluster. If error bars are drawn, these indicate the range of scaled step-out frequencies measured at different field strengths ($n = 38$).

rotations, increases with the angular velocity of the field, such that

$$\theta = \begin{cases} \arcsin\left(\dfrac{\omega_{\mathrm{f}}}{\omega_{\mathrm{so}}}\right), & \text{permanent magnet,} & \text{(4a)} \\[2ex] \dfrac{1}{2}\arcsin\left(\dfrac{\omega_{\mathrm{f}}}{\omega_{\mathrm{so}}}\right), & \text{soft magnet.} & \text{(4b)} \end{cases}$$

Figure 4C shows the phase angle of the clusters increases with the angular velocity ω_{f} of the field. The permanent magnet model captures the phase difference between the cluster and the field. However, the measured phase angles are greater than the calculated results of the model. This difference is attributed to the direction of the magnetic moment. While the preferred magnetization direction is measured in a DC field, the shape, and thereby the magnetic moment, of the clusters change slightly due to the viscous drag force when the clusters start to rotate.

As the clusters oscillate when they are actuated above their step-out frequency, their average angular velocity decreases. For both permanent and paramagnetic objects [63, 64], the average angular velocity is given by

$$\frac{\omega_{\mathrm{c}}}{\omega_{\mathrm{f}}} = 1 - \sqrt{1 - \left(\frac{\omega_{\mathrm{so}}}{\omega_{\mathrm{f}}}\right)^2}. \tag{5}$$

Figure 4D shows that (5) captures the behavior of the clusters in terms of their average angular velocity. Below the step-out frequency, no oscillations are present and the angular velocity of the cluster is equal to the angular velocity of the magnetic field. Above the step-out frequency, the angular velocity of the clusters decreases rapidly, to less than 20% of the angular velocity of the field at twice the step-out frequency.

The step-out frequency required to model the movement of a cluster is measured experimentally. For permanently magnetic objects, their step-out frequency is given by $\omega_{\mathrm{so}} = |\mathbf{m}||\mathbf{B}|/f_{\mathrm{r}}$. However, the magnetization of the individual clusters is unknown. Ideally, the step-out frequency is predicted based on the properties of the cluster. To find an expression for the step-out frequency of a cluster, the cluster is approximated as a soft-magnetic ellipsoid (figure 3A). The step-out frequency is then given by [65]

$$\omega_{\mathrm{so}} = \frac{|\mathbf{B}|^2\,|n_{\mathrm{a}} - n_{\mathrm{r}}|\,V}{2\mu_0 n_{\mathrm{a}} n_{\mathrm{r}} f_{\mathrm{r}}}. \tag{6}$$

where V is the volume of the ellipsoid and μ_0 is the permeability of free space. The step-out frequency scales with the square of the field strength. Note that the demagnetizing factors [66] and the rotational drag coefficient [67] of a prolate ellipsoid rotating about one of its radial axes are known. Substitution of these coefficients into (6) shows that the step-out frequency is independent of the volume of the ellipsoid, and solely dependent on the ratio between its axis of symmetry and its radial axes $R = a/b > 1$, such that

$$\frac{\omega_{\mathrm{so}}}{|\mathbf{B}|^2} = \frac{|n_{\mathrm{a}} - n_{\mathrm{r}}|}{16\eta\mu_0 n_{\mathrm{a}} n_{\mathrm{r}}}\frac{(4R^3 - 2R)\ln\left(R + \sqrt{R^2 - 1}\right) - 2R^2\sqrt{R^2 - 1}}{(R^4 - 1)\sqrt{R^2 - 1}}, \tag{7}$$

where η is the viscosity of the surrounding fluid. Figure 4E shows the step-out frequency, scaled with the square of the applied field strength as dictated by (7), versus the aspect ratio R of the clusters. Scaling the step-out frequency with the square of the field strength results in an average normalized root-mean-square error (NRMSE) of 31% within a cluster. No correlation between R and the scaled step-out

frequency is found. The scaled step-out frequency differs by a factor $\mathcal{O}(10^3)$ between clusters, and the step-out frequency of a cluster could alter slightly. One possible explanation for these findings is that clusters have different step-out frequencies due to their different magnetic moments and viscous drag coefficients. The volume, orientation, and distribution of the nanoparticles determine the magnetic moment of a cluster. Additionally, the geometry and orientation of the cluster, and effects of the environment, such as the effect of a nearby surface [68–70] or fluid heterogeneity, determine the viscous drag experienced by a cluster. The lack of correlation between R and the step-out frequency, can also be explained by the permanent magnet model, which does not dictate a relationship between R and the step-out frequency. Further, measurements show that 95% of the clusters have a step-out frequency below the soft-magnetic model prediction, for $\eta = 0.001$ Pa s. While the model assumes a solid paramagnetic ellipsoid, the IRONSperm clusters consist of ferromagnetic nanoparticles and sperm cells, resulting in much less magnetic material. Figure 4F shows that there is no relation between the estimated volume of a cluster and its scaled step-out frequency. This behavior is also predicted by both the soft- and permanent-magnet models, as the drag coefficient of an object and the amount of magnetic material both increase with the volume.

4. Rolling Velocity of the Clusters

The rotational motion of a cluster in a rotating magnetic field can be used for locomotion. As it is likely that a cluster is close to a boundary, rolling is a convenient locomotion mechanism. When a cluster is in contact with a surface, applying a magnetic field rotating about an axis in the x-y plane causes the cluster to roll. Figure 5A shows a cluster rolling as the magnetic field rotates about the x-axis (video S5 in supplementary material). During rolling without slipping, an object travels the length of its perimeter p in one rotation, i.e., the rolling velocity v scales linearly with the perimeter of the object and the actuation frequency, such that $v = p\omega_{\mathrm{f}}/(2\pi)$. The top graph in figure 5B shows that the rolling velocity of the clusters increases linearly with the actuation frequency up to approximately 0.4 Hz. Above this value, the rolling velocity further increases nonlinearly. Clusters with a larger perimeter move faster than clusters with a smaller perimeter at the same actuation frequency. A maximum rolling velocity of 563 µm/s is achieved by a cluster with an estimated circumference of 195 µm under the influence of actuating field at frequency of 10 Hz. The bottom graph in figure 5B shows that the rolling velocity scaled by the actuation frequency and cluster perimeter, i.e., the number of perimeters traveled by a cluster per rotation of the magnetic field, decreases with the actuation frequency. The prediction based on rolling without slipping is an upper limit for the rolling velocity. Only at low frequencies do the clusters approach this limit. We hypothesize that at larger actuation frequencies, the clusters start slipping on the surface. Possibly, hydrodynamic lift is generated at high frequencies [71], such that clusters no longer experience enough traction to roll.

During rolling, the clusters can be steered in 2D space, by changing the rotation axis of the field (figure 5C, video S6 in supplementary material). At $t = 0$ s, the field is rotating about the y-axis at 3 Hz. At $t = 2.4$ s, the field is rotating about the x-axis and the cluster turns. As the clusters have a preferred orientation in the magnetic field (section 3), the clusters turn, instead of switching their rotation axis, when changing the rotation axis of the external field. At $t = 4.6$ s, the field is rotating
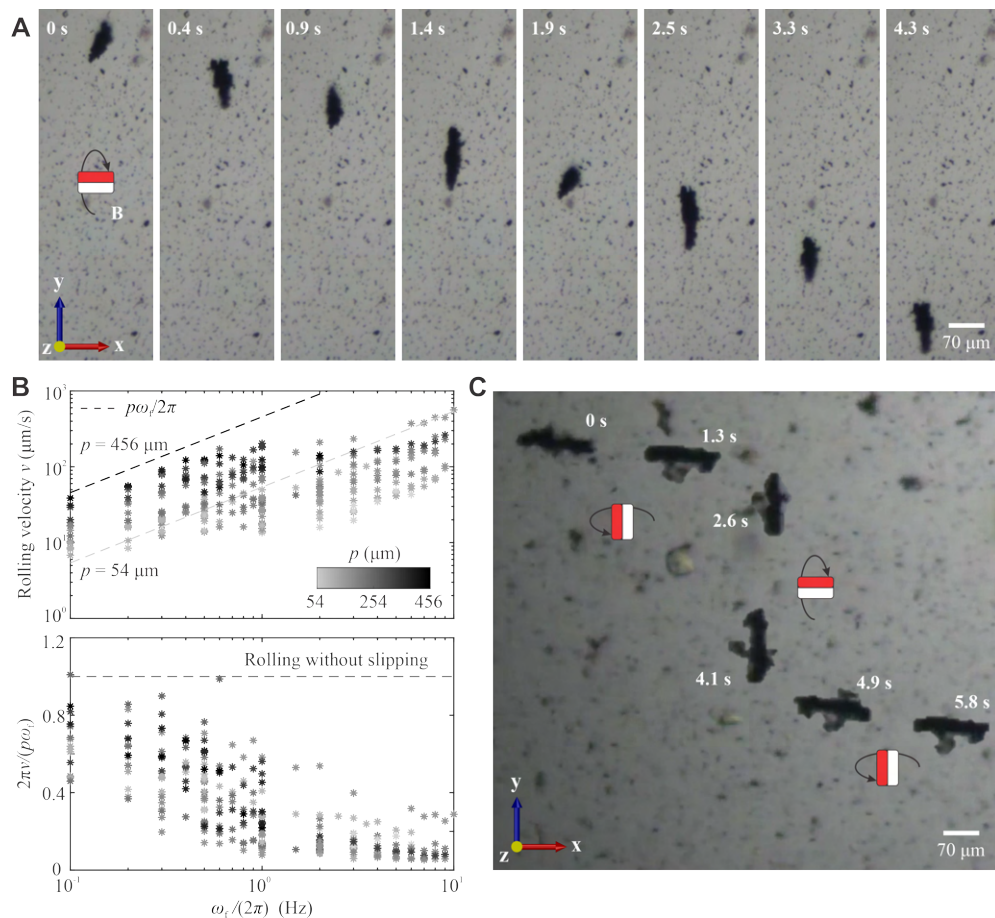
Figure 5. IRONSperm clusters can roll over a surface and can be steered by controlling the field-rotation axis in the **xy**-plane. **(A)** An IRONSperm cluster rolls on a surface at a velocity of 110 µm/s under the influence of a magnetic field of 4 mT rotating at 0.5 Hz about the **x**-axis. **(B)** Top: The rolling velocity of the clusters increases non-linearly with frequency. Larger clusters roll faster than smaller clusters at the same actuation frequency ($n = 35$). Bottom: The number of perimeters traveled per field rotation decreases with actuation frequency ($n = 35$). **(C)** By changing the field-rotation axis, the cluster is steered to roll along a prescribed path. The cluster changes direction with approximately 9 rad/s. In this image, the cluster moves at 140 µm/s as it is actuated by a 6 mT magnetic field rotating at a frequency of 3 Hz.

about the y-axis again and the cluster turns. The clusters change direction with up to 9 rad/s, depending on their magnetic moment and viscous drag coefficient.
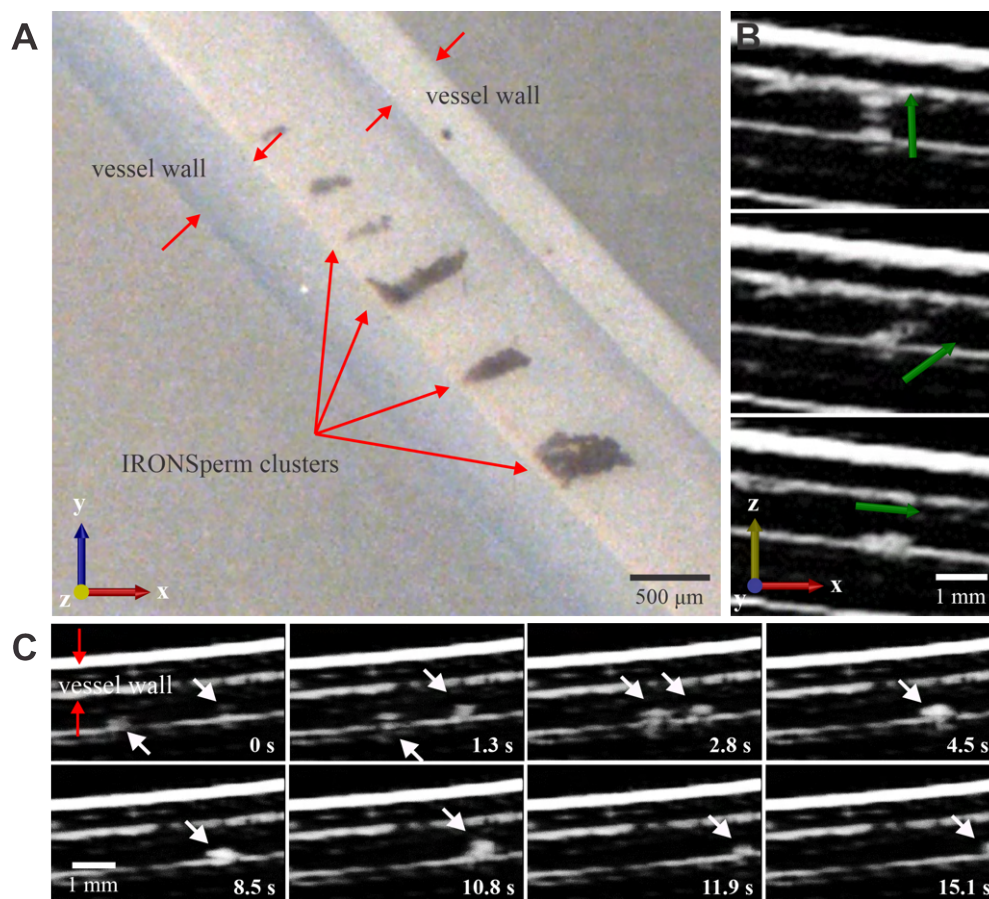
Figure 6. The IRONSperm clusters are localized using ultrasound images. **(A)** The clusters used during the ultrasound experiments are less than 800 μm in length. Due to clustering their size changed during the experiments. **(B)** The orientation of this 800-μm-long cluster is estimated from ultrasound images within 20° using 14 MHz ultrasound waves at a distance of approximately 0.5 cm. The green arrow represents the magnetization direction. **(C)** The clusters with a diameter of 500 μm are tracked during magnetic actuation using 14 MHz ultrasound waves at a distance of approximately 0.5 cm. The white arrows indicate the clusters. At $t = 4.5$ s, two IRONSperm clusters merged and continued rolling together. The merge increased their echogenicity by 50%.

5. Localization of IRONSperm Clusters Using Ultrasound Imaging

The movement of the clusters can be followed easily under a microscope *in vitro*, but *in vivo*, optical imaging modalities cannot be used and instead medical imaging modalities such as ultrasound are required. Ultrasound waves travel through a medium at a velocity c, depending on the density of the medium. When a wave encounters an acoustic impedance mismatch, part of the wave is reflected. Due to the iron nanoparticles in the IRONSperm clusters, the clusters have a different acoustic impedance from their surroundings. Detecting the reflected ultrasound waves makes IRONSperm clusters visible on ultrasound images. The axial resolution of ultrasound
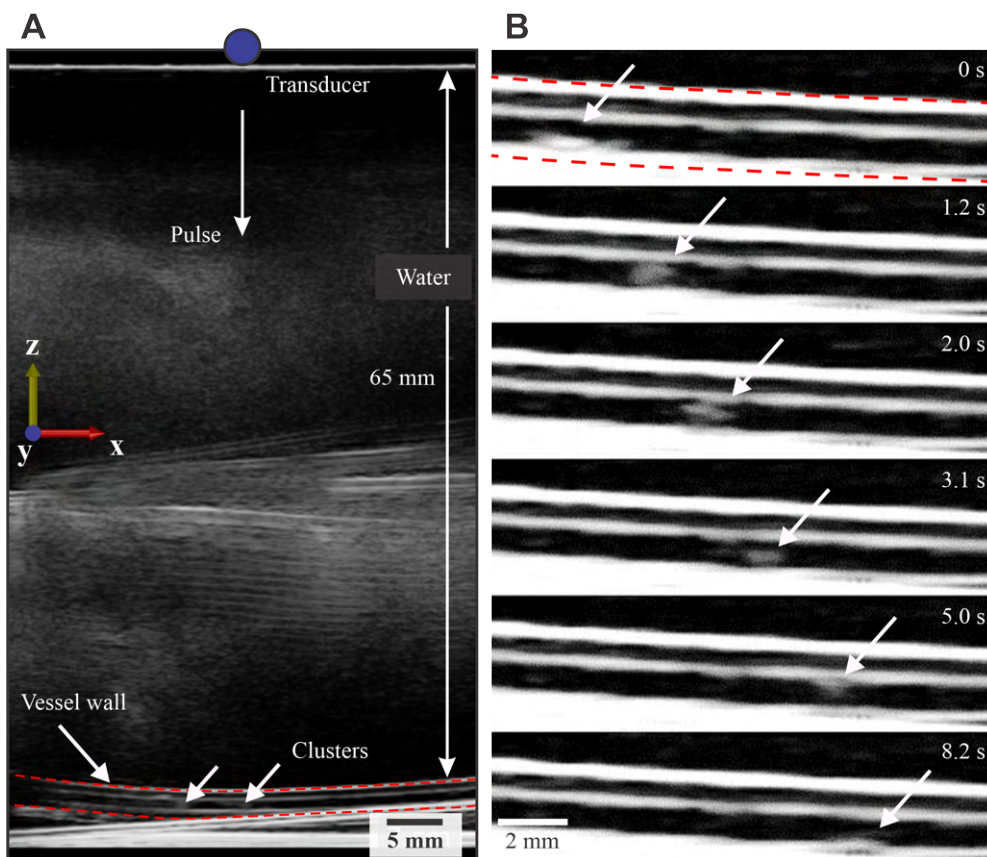
Figure 7. Localization of IRONSperm clusters by ultrasound is achieved at relatively large penetration depth. **(A)** The clusters are detectable using 10 MHz ultrasound waves at a distance of approximately 6.5 cm. **(B)** The clusters are localized during magnetic actuation at a distance of 6.5 cm. The white arrow indicate a cluster rolling at approximately 1 mm/s, while actuated at frequency of 1 Hz.

imaging is equal to the wavelength, λ, of the used ultrasound waves [72]. This wavelength is given by $\lambda = c/f$, where f is the frequency of the ultrasound waves. In tissue, $c \approx 1540$ m/s. Therefore, a cluster with a diameter of 500 µm (figure 6A), can be detected using an ultrasound frequency of at least 3 MHz. From a penetration depth of 5 mm and using an ultrasound frequency of 14 MHz, the orientation of a cluster with a diameter of 800 µm can be estimated within approximately 20° on the ultrasound images (figure 6B, video S7 in supplementary material). Figure 6C shows that the motion and time-varying orientation of the clusters during rolling improves the contrast of the clusters in the ultrasound images. As shown in section 3, clusters can merge and in this case the contrast of the two clusters at $t = 4.5$ s is improved, i.e., pixel intensity, by 50% (video S8 in supplementary material) and the larger resulting size enables easier detectability.

Note that the experimental actuation and localization results shown in figure 6 are achieved with a small distance between the ultrasound transducer and the cluster. For practical medical applications, it is necessary to localize the cluster at greater

penetration depths as the microrobots need to access deeper tissues. The penetration depth of ultrasound waves increases with their wavelength [72]. As larger clusters remain visible when a larger ultrasound wavelength is used, larger clusters are detectable at larger depths. Figure 7A shows that IRONSperm clusters with a diameter of 500 µm are visible at a distance of 65 mm, the maximum setting of the used ultrasound probe. During this localization trial, the clusters are actuated using a 1 Hz rotating magnetic field to move at approximately 1 mm/s (video S9 in supplementary material). While the clusters can be followed, the decreased ultrasound frequency of 10 MHz lowers the spatial resolution. The detectability of the clusters is dependent on their orientation with respect to the ultrasound transducer. During rolling, the orientation of the cluster alters continuously, improving detectability of clusters that have an axis which is too short to be detected [73]. To ensure that the cluster is continuously visible during rolling, each axis of the cluster should be long enough to be detectable. This length is dependent on the used ultrasound settings.

6. Drug Loading of the Clusters

IRONSperm clusters can be magnetically actuated and localized using ultrasound imaging simultaneously. These are the first steps for the intended *in vivo* biological application. When IRONSperm clusters are incubated with the anticancer drug doxorubicin hydrochloride (DOX-HCl), the sperm cells absorb this drug through their cell membrane (figure 2A). After one hour of incubation of the particle-coated sperm cells with this drug, the cells take up an average of 4.29 pg DOX-HCl per cell. This is in agreement with previously reported amounts of drugs per sperm cell [45].

The DOX-HCl is fluorescent, so the drug-loaded sperm cells in the clusters can be visualized using fluorescent microscopy. The cytosol volume of the head is much larger than that of the flagellum, so that the drug is mostly present in the head, visible by the strong fluorescent signal of the sperm heads in the images. These areas in the cluster that contain magnetic nanoparticles, do not contain drugs, and do not emit fluorescent signals, as shown in figure 8A and B, which display 3D reconstructions of 2 different clusters. The red dots show the distribution of the drug-loaded sperm cells within the cluster. Note that the cluster in figure 8A is a densely packed agglomerate that displays the majority of the drug-loaded sperm cells on the surface of the cluster. The density of the cluster can be recognized by the strong contrast of the cluster in the bright-field image figure 8A. Here, there is no space between the sperm cells and a higher amount of magnetic particles might have led to the tight packing of the cluster. One reason why fluorescent cells can only be seen in the perimeter of the cluster is that the fluorescent signal from any cells in the center are blocked by the cluster itself. This might be due to the mechanism of clustering, which arranges the cell-particle agglomerate in a way that the magnetic material is agglomerating stronger in the center of the cluster under the influence of the rotating magnetic field, while the cell heads orient towards to outer area of the cluster.

The display of the drug-loaded cells on the surface of the magnetic cluster has the benefit of enhancing the drug availability to the target. In figure 8B (video S10 in supplementary material), the 3D reconstruction of another cluster is shown from different angles. It can be seen that the sperm cells and the DOX-HCl are distributed fairly uniformly over the entire cluster. This cluster might contain a lower density of magnetic material and hence did not agglomerate as tightly. In this case, all fluorescent cells are visible throughout the cluster without blocking of the fluorescent
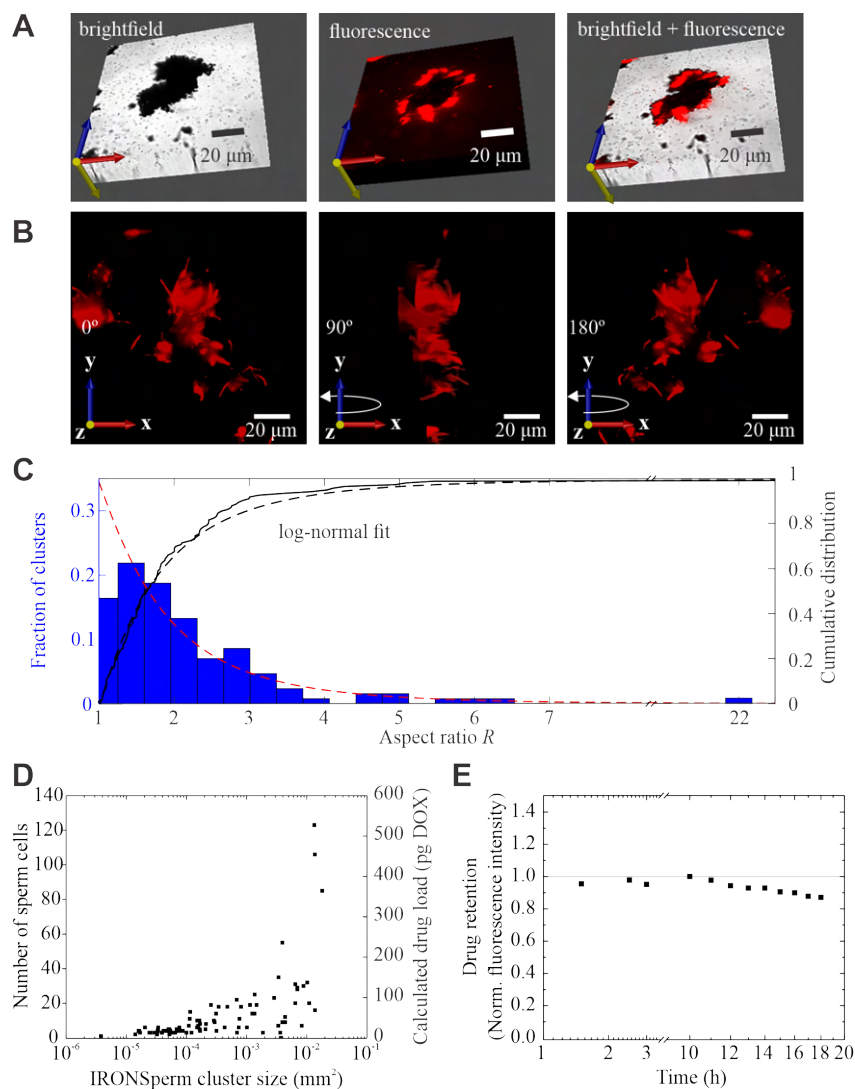
Figure 8. IRONSperm clusters of different shapes and sizes are loaded with drugs. **(A)** 3D reconstruction of a Z-stack of an IRONSperm cluster from bright-field (BF), fluorescent (FL) and BF-FL-overlayed images. **(B)** 3D reconstruction of an IRONSperm cluster from fluorescent z-stacks (50 slices) from different angles (0°, 90° and 180°). DOX-HCl-loaded bovine sperm appear red in fluorescent channel. The DOX-HCl is distributed over the whole cluster. **(C)** Distribution of the aspect ratio of clusters ($n = 128$). The red dashed line is a fitted folded log-normal probability density function, scaled to match the histogram. Most clusters have an aspect ratio below 3. **(D)** Number of cells (left y-axis) and respective calculated drug load (right y-axis) per IRONSperm cluster ($n = 88$). Cluster size was measured by area per 2D image. In general, the number of cells increases with cluster size, but the large spread indicates different cell densities. **(E)** Drug retention of DOX-HCl-loaded clusters over time. Drugs can be retained for more than 10 hours, after which a 20% decrease is seen in the next 10 hours.

signal due to a looser agglomeration of the IRONSperm. We can assume that with

increasing exposure to rotating magnetic field, the density of the cluster increases due to prolonged magnetic attraction between the magnetic elements inside the cluster and the interaction with the environment which leads to denser agglomeration. At the same time, more IRONSperm are added to the cluster, so that the size is also increasing over time.

The IRONSperm clusters vary in their shape and size (figure S11 in supplementary material). Their aspect ratio R follows a log-normal distribution with a mode of 1.7 and a standard deviation of 2.1 (figure 8C, $n = 128$). There are a few clusters with an aspect ratio higher than 4. These are mostly clusters with a few sperm cells (less than 25 cells), so that the aspect ratio of single bovine sperm cell (ca. 1:60) plays a role in the resulting elongated cluster. As shown in section 3, aspect ratio is not important for actuation. However, it could influence the drug release based on the surface area of the cluster. Cluster dimensions vary between 18 and 607 µm ($n = 128$). The importance of cluster size for locomotion is addressed in section 4. For drug loading, cluster size is important because the number of sperm cells increases with cluster size (figure 8D). Since the sperm cells are loaded with the drugs prior to clustering, a uniform loading is guaranteed. Hence, the drug load increases approximately proportional to the number of cells in the cluster. However, cell density varies among clusters and this variation increases with cluster size. As the analyzed clusters contained up to 120 sperm cells, theoretically a load of up to 500 pg DOX-HCl per cluster could be achieved. Not only can the clusters be loaded with drugs, the IRONSperm clusters also retain the drugs for up to 10 hours (figure 8E). This is possible because the biomembrane of the cells takes up the drug easily and contains it stably inside the cytosol. After 10 hours, a slight decrease in fluorescence intensity of approximately 2% per hour is observed for the next 10 hours.

7. Discussions

Contrary to the non-biohybrid microrobot collectives researched previously [50–57], the IRONSperm clusters do not rely solely on an external input to bundle together. While a magnetic field is used to initially aggregate clusters, the IRONSperm clusters are able to stay connected due to the entanglement and stiction forces between the sperm cells that act as flexible magnetic filaments. The properties of biological cells assist in the control of microrobots [36]. While the biological stiction force eases the formation of IRONSperm clusters, it also prevents the clusters to reconfigure their structure or even break up into smaller clusters. This ability would be useful to access hard-to-reach locations, as shown with previously developed microrobot swarms [50, 52].

To actuate a cluster, the step-out frequency is determined by finding the frequency at which the cluster start to oscillate. Other measurable parameters, such as the average angular velocity during oscillations [74], the phase angle when moving in sync with the magnetic field, or the oscillation frequency can also be used to find the step-out frequency. However, predicting the step-out frequency based on cluster appearance would be ideal. The paramagnetic ellipsoid model provides an upper bound for the step-out frequency of the clusters, but improved estimates of the drag coefficient and magnetic moment of IRONSperm clusters could lead to more accurate step-out frequency predictions.

Rolling locomotion allows IRONSperm clusters to move at speed of 500 µm/s, fifty times faster than the swimming velocity of an individual IRONSperm, tackling the

disadvantage of slow locomotion speeds of the individual IRONSperm [45]. However, this locomotion strategy requires a surface to roll on, whereas the IRONSperm can swim in the bulk fluid. The achieved rolling velocity is faster than the 300 µm/s achieved with magnetotactic bacteria swarms [58, 75], but slower than the 42 mm/s achieved with disk-shaped non-hybrid microrobots of similar size to the IRONSperm clusters [52].

In future work, further measurements of the magnetization, drag coefficient and stiction forces of IRONSperm clusters could provide more accurate predictions of the behavior of IRONSperm cluster. With this knowledge, the building of clusters with specific shapes and sizes, and the reshaping, combining and splitting of clusters can be investigated. Disconnecting individual IRONSperm from the cluster, to actuate IRONSperm to swim instead of roll, could allow for locomotion when no rolling surface is available. The wide range of step-out frequencies among clusters could prove useful for simultaneous actuation of multiple clusters [65] at different rolling velocities under the influence of the same magnetic field. Further, the ability to move through complex environments, such as vasculature and cavities would be of high interest in order to evaluate their *in vivo* application potential. While the actuation of the clusters in this study was done at relatively short distance, stronger magnetic fields could facilitate long-range actuation. The drug retention of IRONSperm clusters is longer compared to liposomes, which usually start releasing up to 30% of the drug over the first two hours [76]. However, compared to liposomes, the drug loading amount of IRONSperm clusters could still be increased. Controlled drug release mechanisms would complement the drug loading and retention well. Possible approaches to achieve this would be to conjugate the magnetic nanoparticles with cell-specific antibodies, which are then only targeting cells of interest (e.g., cancer cells). In combination with ultrasound, sonoporation, the ultrasound-based permeabilisation of the sperm cell membranes, could also be of interest [77].

Finally, combining living sperm cells with magnetic nanoparticles results in novel explorative microrobotic tools, which could be used for new purposes. It enables the visualization of sperm swarms *in vivo* which is an important tool for the investigation of *in vivo* processes. The ability to make swarms of spermatozoa visible using ultrasound imaging provides a new tool for the study of sperm migration, to understand how long and where sperm cells remain inside the reproductive tract. Currently, such sperm tracking towards the fertilization site is not possible in a non-invasive manner. Besides the application in reproductive science, biohybrid microrobots could be used to act as deep vessel delivery machines or diagnostic tools.

8. Conclusions

In this work, we fabricate drug-loaded biohybrid clusters and understand their characteristics to enable wireless rolling locomotion and noninvasive localization simultaneously. Nanoparticle-coated sperm cells electrostatically and magnetically entangle in dense clusters of up to 120 cells, with dimensions between 20 and 600 µm and cell density variation by an order of magnitude. Despite the cell density variation between clusters and their complex internal structure, the movement of a cluster in a rotating magnetic field is captured by a permanent magnet model, using the step-out frequency of the cluster, owing to the remanence magnetization of the clusters. A soft-magnetic ellipsoid model predicts a step-out frequency of the clusters based on their aspect ratio, but overestimates 95% of the cases. In reality, the step-out

frequency of the clusters is independent of the aspect ratio and volume of the clusters. Consequently, permanent magnet models will likely be the best choice in real-time motion control. As proof of concept, the cluster are steered controllably by magnetic actuation below their step-out frequency, and achieve rolling velocities of 500 µm/s at an actuation frequency of 10 Hz. The rolling velocity increases nonlinearly with the actuation frequency of the field and cluster perimeter. During actuation, the clusters are visible on ultrasound imaging, in contrast to individual IRONSperm. At a distance of 65 mm, clusters with a diameter of 500 µm remain detectable while traveling at 1 mm/s. A potential application of the IRONSperm clusters is targeted drug delivery. As a demonstration, the sperm cells in the clusters were loaded with DOX-HCl. The largest cluster contained up to 120 cells and could theoretically contain up to 500 pg of DOX-HCl. Based on fluorescence intensity measurements, the drugs were retained for up to 10 hours, with a 20% reduction in the next 10 hours. The aggregation of drug-loaded microrobots, and their collective actuation and localization potential demonstrated in this study place emphasis on the importance of the investigation and development of collective microrobots and their potential for *in vivo* applications.

9. Materials and Methods

9.1. Fabrication of Biohybrid IRONSperm

Sperm-templated microrobots were fabricated by an electrostatic-based self-assembly of iron oxide nanoparticles and sperm cells [45]. Cryopreserved bovine semen straws were obtained from Masterrind GmbH Meißen and stored in liquid nitrogen. The semen straws were thawed in a 37°C water bath for 2 minutes, before diluting the semen in 1 mL SP-TALP (Caisson labs). The sperm sample was centrifuged at 300 g for 5 minutes, the supernatant removed and resuspended in distilled water. This washing step was repeated twice before adding the elongated 150 nm long maghemite rice grain-shaped nanoparticles. The sperm cells die in the process. Samples were stored at 5°C and agglomeration of the cells enables formation of the clusters.

9.2. Magnetic Moment and Step-Out Frequency Characterization

Suspensions of IRONSperm clusters in distilled water with approximately 1.7×10^5 cells/ml were used to measure the magnetic moment using a vibrating sample magnetometer (VSM) from Oxford Instruments. The suspension is contained inside a plastic container and a polyetheretherketone sample holder. The collected magnetization data (figure S2 in supplementary material) show hysteretic effects within the range of external magnetic field of ±2 T and a magnetic coercivity of 41 mT.

The step-out frequencies of IRONSperm clusters were characterized using a triaxial Helmholtz coil system. The Helmholtz coils generate a maximum magnetic field of 8 mT and maximum rotational frequencies of 10 Hz. Optical images were captured at 30 fps using a microscopic unit (MF-B Series 176 Measuring Microscopes, Mitutoyo, Kawasaki, Japan) and camera (avA1000-120kc, Basler Area Scan Camera, Basler AG, Ahrensburg, Germany). Cluster with various sizes were analyzed using 3x, 10x and 20x Mitutoyo phase objectives. IRONSperm samples of approximately 3 µL were analyzed in this setup. IRONSperm concentrations between approximately 1.2×10^2 and 1.8×10^3 cells/µL were used. In each trial, existing IRONSperm clusters

were localized, or new clusters were formed by applying rotating magnetic field of 8 mT at frequency of 0.1 Hz or by rolling the IRONSperm clusters on the surface to enable agglomeration with a neighboring cluster. The magnetic field-rotation axis was set perpendicular to the surface (figure 3A, z-axis). An initial field strength was adjusted based on the magnetic response of the cluster. A DC field was applied to determine the preferred magnetization axis of each cluster. The clusters were actuated at a frequency range between 0.1 and 10 Hz until the magnetic torque was no longer sufficient to keep them in synchrony with the field, i.e., the step-out frequency was reached. The actuation frequency was increased with steps of 0.1 Hz. The field strength was increased and again the step-out frequency was measured by increasing the field frequency. The phase angle was measured at approximately ten points in time over a period of multiple cluster rotations to find an average phase angle. The angular velocity of the clusters was measured over multiple field rotations. Step-out frequency characterization data were collected using 38 IRONSperm clusters. Each cluster was traced with an ellipse to estimate its axis lengths and aspect ratio R, as shown in figure 3. The volume of each cluster was estimated using the volume of a prolate ellipsoid, $\frac{4}{3}\pi ab^2$. The phase lag of 18 of the 38 clusters was measured, as the preferred magnetization axes of these clusters were clearly distinguishable. The angular velocity of 27 of the 38 clusters was estimated, as these clusters were actuated at a low enough frequency to prevent aliasing of the used camera.

Differential equation (3) was simulated in MATLAB2019B using the forward Euler method with a timestep of 0.001. For the initial conditions, the values of the first measurement of the field and cluster direction were used.

9.3. Rolling Velocity

A field strength of 5-8 mT was chosen such that each cluster was actuated below its step-out frequency. The rotation axis of the field was set parallel to the surface (figure 3A, y-axis). Clusters were recorded while rolling through a workspace of 1.7 mm × 1.3 mm at field frequencies between 0.1 and 10 Hz. The velocity of each cluster was calculated from straight runs ($n = 36$). The maximum perimeter of each cluster in the plane defined by the direction of movement and the vector perpendicular to the rolling surface was measured. This perimeter was estimated by measuring the diameter of the cluster in the direction of movement while the magnetic field was parallel to the surface and while the field was perpendicular to the surface. By assuming a rectangle, the maximum possible perimeter of the cluster was estimated as 2 times the sum of these diameters.

9.4. Localization of IRONSperm Clusters Using Ultrasound Images

IRONSperm clusters were injected in a polyethylene vessel with a wall diameter of 1 mm and an inner diameter of 1 mm. This vessel was submerged in water to achieve air-free coupling between the vessel and the ultrasound transducer. A Clarius L15 HD ultrasound transducer was fixed above the vessel, at penetration depth (height) of 5 mm and 65 mm. At a penetration depth of 5 mm, 14 MHz ultrasound waves were used to localize clusters with a diameter of 500 µm. At 65 mm, 10 MHz ultrasound waves were used. The IRONSperm clusters in the vessel were actuated using a rotating permanent magnet from a distance of approximately 5 cm. The magnet had an adhesive force of approximately 3 kg, and rotated at approximately 1 Hz. Ultrasound

images at a distance of 5 mm were recorded at 24 fps. Ultrasound images at a distance of 65 mm were recorded at 15 frames per second.

9.5. Drug Loading

Drug loading experiments were performed with the anti-cancer drug doxorubicin hydrochloride (DOX-HCl). 10 µL of 1 mM DOX-HCl was mixed with 10 µL IRONSperm solution (2.3×10^5 cells) and 100 µL sterile water. The solution was mixed on a rotary wheel for one hour at room temperature, protecting it from light by covering the vial in aluminum foil. Three replicate samples were prepared. The IRONSperm concentration was determined by cell counting in a Neubauer chamber and calculated using a stock concentration of 2.3×10^7 cells/mL. Subsequently, one mL of water was added to the sample and centrifuged at 3000 rpm for 5 minutes to separate the supernatant from the IRONSperm. The supernatant was then measured in a SPARK plate reader, along with a standard row of DOX-HCl (0-10 µM) and reference solutions, that did not contain any IRONSperm. The fluorescence intensity was measured in 96 well plates by applying a 480 nm excitation and 590 nm emission.

The aspect ratios R of the clusters were obtained by measuring the longest and shortest diameter of the clusters in images obtained from bright-field microscopy. Tracing the circumference of the clusters in the images gave the cluster area. The number of cells in each cluster of 88 clusters was counted manually in the fluorescent images. A folded log-normal distribution was fitted to the aspect ratio distribution of the clusters.

Time-lapse imaging of IRONSperm clusters was used to determine the release of the drugs from IRONSperm over time. Z-Stacks of differential interference contrast and fluorescence channel of the IRONSperm clusters were performed every 30 minutes over a whole duration of 18 hours in aqueous solution. From the total fluorescence intensity per time point, the drug retention inside the cluster was estimated.

Conflict of Interest: The authors declare no conflict of interest.

Author Contributions: K.I.N.A.M. developed the theoretical model, designed and performed the actuation and ultrasound experiments, analyzed the data, and wrote the manuscript. V.M. conceived and designed the microrobots, designed and performed the microscopic imaging and drug loading experiments, and participated in writing and editing the manuscript. L.A. supervised the work of K.I.N.A.M., participated in the design of the actuation and ultrasound experiments, participated in drafting the paper, revised and edited the manuscript. I.S.M.K. supervised the work of K.I.N.A.M., conceived and designed the microrobots, participated in the design of the actuation and ultrasound experiments and revised and edited the manuscript.

References

[1] Sungwoong Jeon, Sangwon Kim, Shinwon Ha, Seungmin Lee, Eunhee Kim, So Yeun Kim, Sun Hwa Park, Jung Ho Jeon, Sung Won Kim, Cheil Moon, Bradley J. Nelson, Jin young Kim, Seong Woon Yu, and Hongsoo Choi. Magnetically actuated microrobots as a platform for stem cell transplantation. *Science Robotics*, 4(30), 5 2019.

[2] Metin Sitti, Hakan Ceylan, Wenqi Hu, Joshua Giltinan, Mehmet Turan, Sehyuk Yim, and Eric Diller. Biomedical Applications of Untethered Mobile Milli/Microrobots, 2 2015.

[3] Bradley J. Nelson, Ioannis K. Kaliakatsos, and Jake J. Abbott. Microrobots for minimally invasive medicine, 7 2010.

[4] Yunus Alapan, Oncay Yasa, Berk Yigit, I. Ceren Yasa, Pelin Erkoc, and Metin Sitti. Microrobotics and Microorganisms: Biohybrid Autonomous Cellular Robots. *Annual Review of Control, Robotics, and Autonomous Systems*, 2(1):205–230, 5 2019.

[5] Zhengxin Yang and Li Zhang. Magnetic Actuation Systems for Miniature Robots: A Review. *Advanced Intelligent Systems*, 2(9):2000082, 9 2020.

[6] Metin Sitti and Diederik S. Wiersma. Pros and Cons: Magnetic versus Optical Microrobots, 5 2020.

[7] Tiantian Xu, Jiangfan Yu, Xiaohui Yan, Hongsoo Choi, and Li Zhang. Magnetic Actuation Based Motion Control for Microrobots: An Overview. *Micromachines*, 6(9):1346–1364, 9 2015.

[8] Stefano Palagi, Andrew G. Mark, Shang Yik Reigh, Kai Melde, Tian Qiu, Hao Zeng, Camilla Parmeggiani, Daniele Martella, Alberto Sanchez-Castillo, Nadia Kapernaum, Frank Giesselmann, Diederik S. Wiersma, Eric Lauga, and Peer Fischer. Structured light enables biomimetic swimming and versatile locomotion of photoresponsive soft microrobots. *Nature Materials*, 15(6):647–653, 6 2016.

[9] Hao Zeng, Owies M. Wani, Piotr Wasylczyk, and Arri Priimagi. Light-Driven, Caterpillar-Inspired Miniature Inching Robot. *Macromolecular Rapid Communications*, 39(1):1700224, 1 2018.

[10] Wei Wang, Luz Angelica Castro, Mauricio Hoyos, and Thomas E. Mallouk. Autonomous motion of metallic microrods propelled by ultrasound. *ACS Nano*, 6(7):6122–6132, 7 2012.

[11] Tailin Xu, Li Ping Xu, and Xueji Zhang. Ultrasound propulsion of micro-/nanomotors, 12 2017.

[12] Rustem F Ismagilov, Alexander Schwartz, Ned Bowden, and George M Whitesides. Autonomous movement and self-assembly. *Angewandte Chemie - International Edition*, 41(4):652–654, 2002.

[13] Maria Guix, Carmen C. Mayorga-Martinez, and Arben Merkoçi. Nano/Micromotors in (Bio)chemical science applications, 6 2014.

[14] Wei Wang, Wentao Duan, Zexin Zhang, Mei Sun, Ayusman Sen, and Thomas E. Mallouk. A tale of two forces: Simultaneous chemical and acoustic propulsion of bimetallic micromotors. *Chemical Communications*, 51(6):1020–1023, 12 2015.

[15] Mahmoud E. Alshafeei, Abdelrahman Hosney, Anke Klingner, Sarthak Misra, and Islam S.M. Khalil. Magnetic-based motion control of a helical robot using

two synchronized rotating dipole fields. In *Proceedings of the IEEE RAS and EMBS International Conference on Biomedical Robotics and Biomechatronics*, pages 151–156. IEEE Computer Society, 9 2014.

[16] Eric Diller, Joshua Giltinan, Guo Zhan Lum, Zhou Ye, and Metin Sitti. Six-degree-of-freedom magnetic actuation for wireless microrobotics. *International Journal of Robotics Research*, 35(1-3):114–128, 1 2016.

[17] Islam S.M. Khalil, Dalia Mahdy, Ahmed El Sharkawy, Ramez R. Moustafa, Ahmet Fatih Tabak, Mohamed E. Mitwally, Sarah Hesham, Nabila Hamdi, Anke Klingner, Abdelrahman Mohamed, and Metin Sitti. Mechanical Rubbing of Blood Clots Using Helical Robots under Ultrasound Guidance. *IEEE Robotics and Automation Letters*, 3(2):1112–1119, 4 2018.

[18] Arthur W. Mahoney, Daniel L. Cowan, Katie M. Miller, and Jake J. Abbott. Control of untethered magnetically actuated tools using a rotating permanent magnet in any position. In *Proceedings - IEEE International Conference on Robotics and Automation*, pages 3375–3380. Institute of Electrical and Electronics Engineers Inc., 2012.

[19] Jürgen Rahmer, Christian Stehning, and Bernhard Gleich. Spatially selective remote magnetic actuation of identical helical micromachines. *Science Robotics*, 2(3), 2 2017.

[20] Patrick Ryan and Eric Diller. Five-degree-of-freedom magnetic control of microrobots using rotating permanent magnets. In *Proceedings - IEEE International Conference on Robotics and Automation*, volume 2016-June, pages 1731–1736. Institute of Electrical and Electronics Engineers Inc., 6 2016.

[21] Tiantian Xu, Gilgueng Hwang, Nicolas Andreff, and Stéphane Régnier. Planar path following of 3-D steering scaled-up helical microswimmers. *IEEE Transactions on Robotics*, 31(1):117–127, 2 2015.

[22] Lidong Yang and Li Zhang. Motion Control in Magnetic Microrobotics: From Individual and Multiple Robots to Swarms. *Annual Review of Control, Robotics, and Autonomous Systems*, 4(1):509–534, 5 2021.

[23] Diana Vilela, Unai Cossío, Jemish Parmar, Angel M. Martínez-Villacorta, Vanessa Gómez-Vallejo, Jordi Llop, and Samuel Sánchez. Medical Imaging for the Tracking of Micromotors. *ACS Nano*, 12(2):1220–1227, 2 2018.

[24] Azaam Aziz, Stefano Pane, Veronica Iacovacci, Nektarios Koukourakis, Jürgen Czarske, Arianna Menciassi, Mariana Medina-Sánchez, and Oliver G. Schmidt. Medical Imaging of Microrobots: Toward in Vivo Applications, 9 2020.

[25] Qianqian Wang and Li Zhang. External Power-Driven Microrobotic Swarm: From Fundamental Understanding to Imaging-Guided Delivery. *ACS Nano*, 15(1):149–174, 1 2021.

[26] Lei Li, Zhiguang Wu, Yiran Yang, Peng Hu, Wei Gao, and Lihong V. Wang. Photoacoustic computed tomography guided microrobots for targeted navigation in intestines in vivo. page 97. SPIE-Intl Soc Optical Eng, 2 2020.

[27] Ana C. Hortelao, Cristina Simó, Maria Guix, Sandra Guallar-Garrido, Esther Julián, Diana Vilela, Luka Rejc, Pedro Ramos-Cabrer, Unai Cossío, Vanessa Gómez-Vallejo, Tania Patiño, Jordi Llop, and Samuel Sánchez. Swarming behavior and in vivo monitoring of enzymatic nanomotors within the bladder. *Science Robotics*, 6(52), 3 2021.

[28] Sylvain Martel and Mahmood Mohammadi. Using a swarm of self-propelled natural microrobots in the form of flagellated bacteria to perform complex micro-assembly tasks. In *Proceedings - IEEE International Conference on Robotics and Automation*, pages 500–505, 2010.

[29] Azaam Aziz, Mariana Medina-Sánchez, Jing Claussen, and Oliver G. Schmidt. Real-Time Optoacoustic Tracking of Single Moving Micro-objects in Deep Phantom and Ex Vivo Tissues. *Nano Letters*, 19(9):6612–6620, 9 2019.

[30] S. Pane, V. Iacovacci, E. Sinibaldi, and A. Menciassi. Real-time imaging and tracking of microrobots in tissues using ultrasound phase analysis. *Applied Physics Letters*, 118(1):014102, 1 2021.

[31] Alonso Sánchez, Veronika Magdanz, Oliver G. Schmidt, and Sarthak Misra. Magnetic control of self-propelled microjets under ultrasound image guidance. In *Proceedings of the IEEE RAS and EMBS International Conference on Biomedical Robotics and Biomechatronics*, pages 169–174. IEEE Computer Society, 9 2014.

[32] Qianqian Wang, Xingzhou Du, Dongdong Jin, and Li Zhang. Real-Time Ultrasound Doppler Tracking and Autonomous Navigation of a Miniature Helical Robot for Accelerating Thrombolysis in Dynamic Blood Flow. *ACS Nano*, page acsnano.1c07830, 1 2022.

[33] Azaam Aziz, Joost Holthof, Sandra Meyer, Oliver G Schmidt, and Mariana Medina-Sánchez. Dual Ultrasound and Photoacoustic Tracking of Magnetically Driven Micromotors: From In Vitro to In Vivo. *Advanced Healthcare Materials*, 10(22):2101077, 11 2021.

[34] Yiwen Feng, Xiaocong Chang, Hao Liu, Ying Hu, Tianlong Li, and Longqiu Li. Multi-response biocompatible Janus micromotor for ultrasonic imaging contrast enhancement. *Applied Materials Today*, 23:101026, 6 2021.

[35] Jinxing Li, Berta Esteban Fernández De Ávila, Wei Gao, Liangfang Zhang, and Joseph Wang. Micro/nanorobots for Biomedicine: Delivery, surgery, sensing, and detoxification, 3 2017.

[36] Leonardo Ricotti, Barry Trimmer, Adam W. Feinberg, Ritu Raman, Kevin K. Parker, Rashid Bashir, Metin Sitti, Sylvain Martel, Paolo Dario, and Arianna Menciassi. Biohybrid actuators for robotics: A review of devices actuated by living cells, 11 2017.

[37] Bahareh Behkam and Metin Sitti. Bacterial flagella-based propulsion and on/off motion control of microscale objects. *Applied Physics Letters*, 90(2):023902, 1 2007.

[38] Morgan M. Stanton, Juliane Simmchen, Xing Ma, Albert Miguel-López, and Samuel Sánchez. Biohybrid Janus Motors Driven by Escherichia coli. *Advanced Materials Interfaces*, 3(2):1500505, 1 2016.

[39] H. W. Huang, F. E. Uslu, P. Katsamba, E. Lauga, M. S. Sakar, and B. J. Nelson. Adaptive locomotion of artificial microswimmers. *Science Advances*, 5(1), 1 2019.

[40] Oncay Yasa, Pelin Erkoc, Yunus Alapan, and Metin Sitti. Microalga-Powered Microswimmers toward Active Cargo Delivery. *Advanced Materials*, 30(45):1804130, 11 2018.

[41] Brian J. Williams, Sandeep V. Anand, Jagannathan Rajagopalan, and M. Taher A. Saif. A self-propelled biohybrid swimmer at low Reynolds number. *Nature Communications*, 5(1):1–8, 1 2014.

[42] Ajay Vikram Singh, Mohammad Hasan Dad Ansari, Mihir Mahajan, Shubhangi Srivastava, Shubham Kashyap, Prajjwal Dwivedi, Vaibhav Pandit, and Uma Katha. Sperm cell driven microrobots-Emerging opportunities and challenges for biologically inspired robotic design, 4 2020.

[43] Veronika Magdanz, Samuel Sanchez, and Oliver G. Schmidt. Development of a sperm-flagella driven micro-bio-robot. *Advanced Materials*, 25(45):6581–6588, 12 2013.

[44] Haifeng Xu, Mariana Medina-Sánchez, Veronika Magdanz, Lukas Schwarz, Franziska Hebenstreit, and Oliver G. Schmidt. Sperm-Hybrid Micromotor for Targeted Drug Delivery. *ACS Nano*, 12(1):327–337, 1 2018.

[45] Veronika Magdanz, Islam S.M. Khalil, Juliane Simmchen, Guilherme P. Furtado, Sumit Mohanty, Johannes Gebauer, Haifeng Xu, Anke Klingner, Azaam Aziz, Mariana Medina-Sánchez, Oliver G. Schmidt, and Sarthak Misra. IRONSperm: Sperm-Templated soft magnetic microrobots. *Science Advances*, 6(28):5855–5863, 7 2020.

[46] Yu Zeng and Bin Liu. Self-propelling and rolling of a sessile-motile aggregate of the bacterium Caulobacter crescentus. *Communications Biology*, 3(1):1–8, 10 2020.

[47] D. J.T. Sumpter. The principles of collective animal behaviour, 2006.

[48] Yasemin Ozkan-Aydin, Daniel I. Goldman, and M. Saad Bhamla. Collective dynamics in entangled worm and robot blobs. *Proceedings of the National Academy of Sciences of the United States of America*, 118(6):2021, 2 2021.

[49] J. Elgeti, R. G. Winkler, and G. Gompper. Physics of microswimmers - Single particle motion and collective behavior: A review. *Reports on Progress in Physics*, 78(5):056601, 4 2015.

[50] Jiangfan Yu, Ben Wang, Xingzhou Du, Qianqian Wang, and Li Zhang. Ultra-extensible ribbon-like magnetic microswarm. *Nature Communications*, 9(1):1–9, 12 2018.

[51] Berk Yigit, Yunus Alapan, and Metin Sitti. Cohesive self-organization of mobile microrobotic swarms. *Soft Matter*, 16(8):1996–2004, 2 2020.

[52] Xiaoguang Dong and Metin Sitti. Controlling two-dimensional collective formation and cooperative behavior of magnetic microrobot swarms. *International Journal of Robotics Research*, 39(5):617–638, 2020.

[53] Zesheng Li, Hongyue Zhang, Daolin Wang, Changyong Gao, Mengmeng Sun, Zhiguang Wu, and Qiang He. Reconfigurable Assembly of Active Liquid Metal Colloidal Cluster. *Angewandte Chemie*, 132(45):20056–20060, 2020.

[54] Li Huang, Louis Rogowski, Min Jun Kim, and Aaron T. Becker. Path planning and aggregation for a microrobot swarm in vascular networks using a global input. In *IEEE International Conference on Intelligent Robots and Systems*, volume 2017-Septe, pages 414–420. Institute of Electrical and Electronics Engineers Inc., 12 2017.

[55] David Cappelleri, Dimitrios Efthymiou, Ashesh Goswami, Nikolaos Vitoroulis, and Michael Zavlanos. Towards mobile microrobot swarms for additive micromanufacturing. *International Journal of Advanced Robotic Systems*, 11, 2014.

[56] Berk Yigit, Yunus Alapan, and Metin Sitti. Programmable Collective Behavior in Dynamically Self-Assembled Mobile Microrobotic Swarms. *Advanced Science*, 6(6), 2019.

[57] Jiangfan Yu, Dongdong Jin, Kai Fung Chan, Qianqian Wang, Ke Yuan, and Li Zhang. Active generation and magnetic actuation of microrobotic swarms in bio-fluids. *Nature Communications*, 10(1):1–12, 12 2019.

[58] Dominic De Lanauze, Ouajdi Felfoul, Jean Philippe Turcot, Mahmood Mohammadi, and Sylvain Martel. Three-dimensional remote aggregation and steering of magnetotactic bacteria microrobots for drug delivery applications. *International Journal of Robotics Research*, 33(3):359–374, 2014.

[59] Veronika Magdanz, Jacopo Vivaldi, Sumit Mohanty, Anke Klingner, Marilena Vendittelli, Juliane Simmchen, Sarthak Misra, and Islam S.M. Khalil. Impact of Segmented Magnetization on the Flagellar Propulsion of Sperm-Templated Microrobots. *Advanced Science*, 8(8):2004037, 2 2021.

[60] Veronika Magdanz, Johannes Gebauer, Priyanka Sharan, Samar Eltoukhy, Dagmar Voigt, and Juliane Simmchen. Sperm-particle interactions and their prospects for charge mapping. *bioRxiv*, page 624510, 5 2019.

[61] Kar W Yung, B Landecker, and Daniel D Villani. An Analytic Solution for the Force Between Two Magnetic Dipoles. *Magnetic and Electrical Separation*, 9:39–52, 1998.

[62] P. A. Valberg and J. P. Butler. Magnetic particle motions within living cells. Physical theory and techniques. *Biophysical Journal*, 52(4):537–550, 10 1987.

[63] Guillermo A. Jorge, María Llera, and Victoria Bekeris. Magnetic particles guided by ellipsoidal AC magnetic fields in a shallow viscous fluid: Controlling trajectories and chain lengths. *Journal of Magnetism and Magnetic Materials*, 444:467–471, 12 2017.

[64] Brandon H. McNaughton, Karen A Kehbein, Jeffrey N Anker, and Raoul Kopelman. Sudden breakdown in linear response of a rotationally driven magnetic microparticle and application to physical and chemical microsensing. *Journal of Physical Chemistry B*, 110(38):18958–18964, 2006.

[65] Arthur W. Mahoney, Nathan D. Nelson, Kathrin E. Peyer, Bradley J. Nelson, and Jake J. Abbott. Behavior of rotating magnetic microrobots above the step-out frequency with application to control of multi-microrobot systems. *Applied Physics Letters*, 104(14):144101, 4 2014.

[66] Jake J. Abbott, Olgaç Ergeneman, Michael P. Kummer, Ann M. Hirt, and Bradley J. Nelson. Modeling magnetic torque and force for controlled manipulation of soft-magnetic bodies. *IEEE Transactions on Robotics*, 23(6):1247–1252, 12 2007.

[67] Francis Perrin. Mouvement brownien d'un ellipsoide-I. Dispersion diélectrique pour des molécules ellipsoidales. *J. Phys. Radium*, 5(10):pp, 1934.

[68] F. Box, K. Singh, and T. Mullin. The interaction between rotationally oscillating spheres and solid boundaries in a Stokes flow. *Journal of Fluid Mechanics*, 849:834–859, 8 2018.

[69] Qianlong Liu and Andrea Prosperetti. Wall effects on a rotating sphere. *Journal of Fluid Mechanics*, 657:1–21, 2010.

[70] A. J. Goldman, R. G. Cox, and H. Brenner. Slow viscous motion of a sphere parallel to a plane wall-I Motion through a quiescent fluid. *Chemical Engineering Science*, 22(4):637–651, 4 1967.

[71] P G Saffman. The lift on a small sphere in a slow shear flow. *Journal of Fluid Mechanics*, 22(2):385–400, 1965.

[72] Alexander Ng and Justiaan Swanevelder. Resolution in ultrasound imaging. *Continuing Education in Anaesthesia, Critical Care and Pain*, 11(5):186–192, 10 2011.

[73] Qianqian Wang, Lidong Yang, Jiangfan Yu, Chi Ian Vong, Philip Wai Yan Chiu, and Li Zhang. Magnetic Navigation of a Rotating Colloidal Swarm Using Ultrasound Images. In *IEEE International Conference on Intelligent Robots and Systems*, pages 5380–5385. Institute of Electrical and Electronics Engineers Inc., 12 2018.

[74] Pietro Tierno, Josep Claret, Francesc Sagués, and Andrejs Cābers. Overdamped dynamics of paramagnetic ellipsoids in a precessing magnetic field. *Physical Review E - Statistical, Nonlinear, and Soft Matter Physics*, 79(2), 2009.

[75] Sylvain Martel, Mahmood Mohammadi, Ouajdi Felfoul, Zhao Lu, and Pierre Pouponneau. Flagellated magnetotactic bacteria as controlled MRI-trackable propulsion and steering systems for medical nanorobots operating in the human microvasculature. *International Journal of Robotics Research*, 28(4):571–582, 4 2009.

[76] Andreas Fritze, Felicitas Hens, Andrea Kimpfler, Rolf Schubert, and Regine Peschka-Süss. Remote loading of doxorubicin into liposomes driven by a transmembrane phosphate gradient. *Biochimica et Biophysica Acta - Biomembranes*, 1758(10):1633–1640, 10 2006.

[77] I. Lentacker, I. De Cock, R. Deckers, S. C. De Smedt, and C. T.W. Moonen. Understanding ultrasound induced sonoporation: Definitions and underlying mechanisms, 6 2014.

A Simulations

A.1 Introduction

To understand IRONSperm clustering, I spent the first months of my thesis simulating (para)magnetic sphere interactions, paramagnetic rod-like structure interactions, Stokes flow, and dipole movement patterns. Whilst these simulation results didn't appear in the final report, they did deepen the understanding of the clustering process. In fact, creating the simulations led to the important theoretical relations between variables presented in the report. Each chapter includes a description of the workings of a simulation, and some results that can be gathered from each simulation. All simulations were done in MATLAB 2019B. The code can be found on my GitHub page [1].

A.2 Spherical Magnetic Dipole Interactions

This 2D simulation simulates N spherical magnetic dipoles in a low reynolds number environment. Each dipole is initialized with a position $\mathbf{p}_i$, i.e. the center of the sphere, a radius R_i and magnetic moment $\mathbf{m}_i$, with $i = 1, 2, ..., N$ (figure A.1A). The resulting movement of the spheres is simulated using the forward Euler method with a variable timestep. Each iteration, the magnetic force $\mathbf{F}_i^{\mathrm{mag}}$ on each dipole i is calculated as the sum of the magnetic forces exerted by all other dipoles [2],

$$\mathbf{F}_i^{\mathrm{mag}} = \sum_{j=1, j \neq i}^{N} \frac{3\mu_0}{4\pi \left\| \mathbf{r}_{ij} \right\|^4} \left(\mathbf{m}_i \left(\mathbf{m}_j \cdot \hat{\mathbf{r}}_{ij} \right) + \mathbf{m}_j \left(\mathbf{m}_i \cdot \hat{\mathbf{r}}_{ij} \right) + \hat{\mathbf{r}}_{ij} \left(\mathbf{m}_j \cdot \mathbf{m}_i \right) - 5\hat{\mathbf{r}}_{ij} \left(\mathbf{m}_j \cdot \hat{\mathbf{r}}_{ij} \right) \left(\mathbf{m}_i \cdot \hat{\mathbf{r}}_{ij} \right) \right), \quad \text{(A.1)}$$

where μ_0 is the vacuum permeability, $\mathbf{r}_{ij}$ is the vector from magnetic dipole j to magnetic dipole i, and $\hat{\mathbf{r}}_{ij}$ is the unit vector in the direction of $\mathbf{r}_{ij}$. A second force, that replicates the existence of a physical volume of the spheres, i.e., the normal force, is given by [3]

$$\mathbf{F}_i^{\mathrm{ev}} = \sum_{j=1, j \neq i}^{N} \frac{3\mu_0}{4\pi \left(R_i + R_j \right)^4} \left\| \mathbf{m}_i \right\| \left\| \mathbf{m}_j \right\| e^{-\xi \left(\frac{\| \mathbf{r}_{ij} \|}{R_i + R_j} - 1 \right)} \hat{\mathbf{r}}_{ij}, \quad \text{(A.2)}$$

where ξ is a constant that dictates the rate of decay of the force. This constant was set to 30. When the distance between two dipoles is the sum of their radii, i.e., the spheres touch, this force is of equal size, but opposite in direction to the maximum magnetic force between the dipoles. If the distance between the dipoles is larger than the sum of their radii, the force diminishes exponentially. A stiction force $\mathbf{F}_i^{\mathrm{stiction}}$ between the spheres was implemented as a spring, to simulate sticky spheres:

$$\mathbf{F}_i^{\mathrm{stiction}} = \sum_{\substack{j=1, j \neq i, \\ \frac{R_i + R_j}{2} < \| \mathbf{r}_{ij} \| < 1.05 \frac{R_i + R_j}{2}}}^{N} -k_s \left(\left\| \mathbf{r}_{ij} \right\| - \frac{R_i + R_j}{2} \right) \hat{\mathbf{r}}_{ij}, \quad \text{(A.3)}$$

where k_s was set to 0.1. Finally, the spheres experience a drag force by the surrounding fluid. In low-Re, this drag force is given by Stokes' law,

$$\mathbf{F}_i^{\mathrm{drag}} = -f_t \mathbf{v}_i, \quad \text{(A.4)}$$

where f_t is the translational drag coefficient of a sphere, given by $6\pi\eta R_i$, where η is the fluid viscosity, and $\mathbf{v}_i$ is the velocity of the sphere. The total force experienced by each dipole (figure A.1B) is given by

$$\mathbf{F}_i^{\mathrm{tot}} = \mathbf{F}_i^{\mathrm{mag}} + \mathbf{F}_i^{\mathrm{ev}} + \mathbf{F}_i^{\mathrm{stiction}} + \mathbf{F}_i^{\mathrm{drag}} = 0. \quad \text{(A.5)}$$
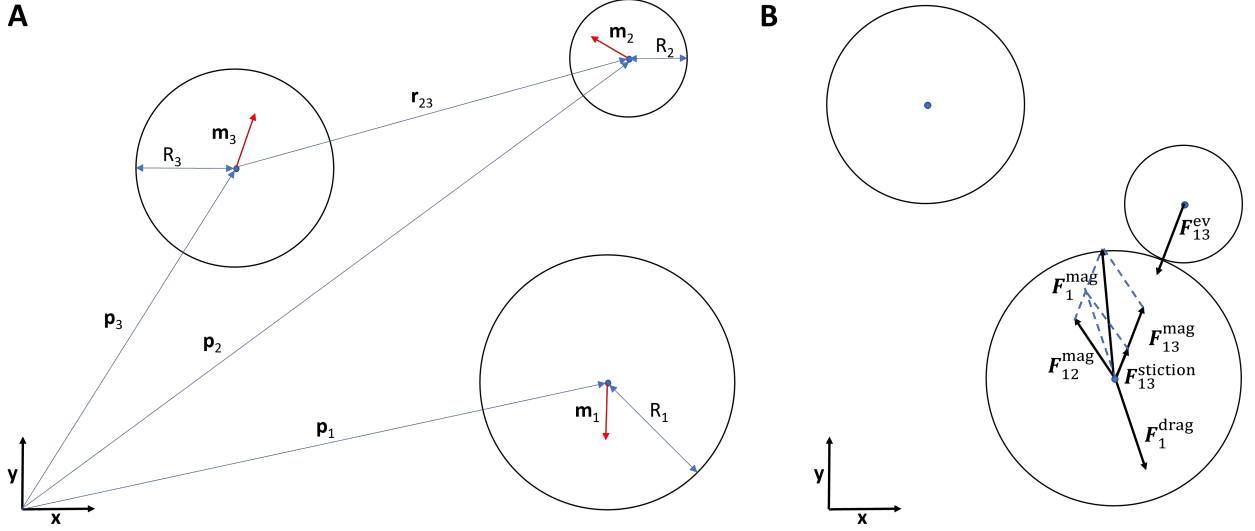
Figure A.1: **(A)** Representation of the variables used to describe the spheres. **(B)** Representation of all the forces acting on the bottom sphere.

No force of the external magnetic field is included, as only uniform magnetic fields were considered during the simulations. The magnetic field on the position of each dipole is the superposition of the external magnetic field and the magnetic fields generated by the other spherical dipoles [4],

$$\mathbf{B}_i = \mathbf{B}_i^{\text{ext}} + \sum_{j=1, j\neq i}^{N} \frac{\mu_0}{4\pi}\left(\frac{3\left(\mathbf{m}_j \cdot \mathbf{r}_{ij}\right)\mathbf{r}_{ij}}{\|\mathbf{r}_{ij}\|^5} - \frac{\mathbf{m}_j}{\|\mathbf{r}_{ij}\|^3} \right), \tag{A.6}$$

where $\mathbf{B}_i^{\text{ext}}$ is the externally applied field at position $\mathbf{p}_i$. For a rotating magnetic field, $\mathbf{B}_i^{\text{ext}}$ is given by $B_{\text{str}}\begin{bmatrix} \cos(\omega_{\text{f}}t) & \sin(\omega_{\text{f}}t) \end{bmatrix}^T$, where B_{str} is the external field strength, ω_{f} is the angular velocity of the field, and t is time. The torque on each dipole due to the external magnetic field and the fields of the other dipoles was given by

$$\tau_i^{\text{mag}} = \mathbf{m}_i^{\perp} \cdot \mathbf{B}_i, \tag{A.7}$$

where $\mathbf{m}_i^{\perp}$ is the vector perpendicular to $\mathbf{m}_i$, rotated 90° counter-clockwise. $\mathbf{a}^{\perp} \cdot \mathbf{b}$ is called the perp dot product or two-dimensional cross product. While the cross product is only defined for three-dimensional vectors, one can regard two-dimensional vectors as vectors on a plane in three dimensions. By adding a third dimension with value 0 to $\mathbf{a}$ and $\mathbf{b}$, the cross product $\mathbf{a} \times \mathbf{b}$ results in $\begin{bmatrix} 0 & 0 & a_1b_2 - a_2b_1 \end{bmatrix}^T$. The perp dot product returns the third dimension of this vector as a scalar. As the stiction force is directed at the center of the sphere, no torque is generated by this force. Finally, the spheres experience a drag torque by the surrounding fluid. In low-Re, this torque is given by [5]

$$\tau_i^{\text{drag}} = -f_r \omega_i, \tag{A.8}$$

where f_r is the rotational drag coefficient for a sphere, given by $8\pi\eta R_i^3$, and ω_i indicates the angular velocity of the sphere. The total torque on each dipole is given by

$$\tau_i^{\text{tot}} = \tau_i^{\text{mag}} + \tau_i^{\text{drag}} = 0. \tag{A.9}$$

The resulting linear velocity of each sphere *relative to the surrounding fluid* due to the experienced force is found by rewriting (A.5),

$$\mathbf{v}_i = \frac{\mathbf{F}_i^{\text{mag}} + \mathbf{F}_i^{\text{ev}} + \mathbf{F}_i^{\text{stiction}}}{6\pi\eta R_i}. \tag{A.10}$$

26

The resulting angular velocity of each sphere *relative to the surrounding fluid* due to the experienced torque is given by rewriting (A.9),

$$\omega_i = \frac{\tau_i^{\text{mag}}}{8\pi\eta R_i^3}. \tag{A.11}$$

However, the forces and torques acting on each sphere induce a fluid flow and vorticity in the surrounding fluid, which has to be taken into account to calculate the (angular) velocity of each sphere in the global reference frame. The velocity of the fluid at the location of sphere i is the sum of the fluid velocities caused by the forces and torques acting on the other spheres. The fluid velocity due to the forces is given by [6]

$$\mathbf{u}_i^{\text{force}} = \sum_{j=1, j\neq i}^{N} \frac{1}{8\pi\eta} \left(\frac{\mathbf{I}}{\|\mathbf{r}_{ij}\|} + \frac{\mathbf{r}_{ij}\mathbf{r}_{ij}^T}{\|\mathbf{r}_{ij}\|^3} \right) \mathbf{F}_j + \frac{R_j^2}{8\pi\eta} \left(\frac{\mathbf{I}}{3\|\mathbf{r}_{ij}\|^3} - \frac{\mathbf{r}_{ij}\mathbf{r}_{ij}^T}{\|\mathbf{r}_{ij}\|^5} \right) \mathbf{F}_j, \tag{A.12}$$

where $\mathbf{I}$ indicates the 2x2 identity matrix and $\mathbf{F}_j = \mathbf{F}_j^{\text{mag}} + \mathbf{F}_j^{\text{ev}} + \mathbf{F}_j^{\text{stiction}}$. The fluid velocity due to the torques on all other spheres is given by

$$\mathbf{u}_i^{\text{torque}} = \sum_{j=1, j\neq i}^{N} \frac{1}{8\pi\eta \|\mathbf{r}_{ij}\|^3} \begin{bmatrix} -r_{ij,y}\tau_j \\ r_{ij,x}\tau_j \end{bmatrix}, \tag{A.13}$$

where $r_{ij,x}$ and $r_{ij,y}$ indicate the x- and y-components of $\mathbf{r}_{ij}$, respectively. The angular velocity of the fluid at the position of sphere i due to the forces on all other spheres is half of the vorticity of the fluid at the position of sphere i,

$$\Omega_i^{\text{force}} = \frac{1}{2} \sum_{j=1, j\neq i}^{N} \frac{1}{4\pi\eta \|\mathbf{r}_{ij}\|^3} \mathbf{F}_j^{\perp} \cdot \mathbf{r}_{ij}, \tag{A.14}$$

where $\mathbf{F}_j^{\perp}$ indicates the vector perpendicular to $\mathbf{F}_j$, rotated 90° counter-clockwise. The angular velocity of sphere i due to the torques on all other spheres is half of the vorticity of the fluid at the position of sphere i,

$$\Omega_i^{\text{torque}} = \frac{1}{2} \sum_{j=1, j\neq i}^{N} \frac{-\tau_j}{8\pi\eta \|\mathbf{r}_{ij}\|^3}. \tag{A.15}$$

In the fluid dynamics, only the first reflections are taken into account, i.e., the fluid flow caused by a sphere alters the movement of the surrounding spheres. In reality, the altered movement of surrounding spheres again alters the movement of the first sphere, and so on [6].

Each iteration k, the position of all particles was updated using the forward Euler method:

$$\mathbf{p}_i^{k+1} = \mathbf{p}_i^k + \left(\mathbf{v}_i^k + \mathbf{u}_i^{\text{force},k} + \mathbf{u}_i^{\text{torque},k} \right) \Delta t^k, \tag{A.16}$$

where Δt^k is the used timestep at iteration k. The orientation of the sphere and thus its magnetic moment was updated using the same method:

$$\mathbf{m}_i^{k+1} = \begin{bmatrix} \cos\left(\left(\omega_i^k + \Omega_i^{\text{torque},k} + \Omega_i^{\text{force},k}\right) \Delta t^k \right) & -\sin\left(\left(\omega_i^k + \Omega_i^{\text{torque},k} + \Omega_i^{\text{force},k}\right) \Delta t^k \right) \\ \sin\left(\left(\omega_i^k + \Omega_i^{\text{torque},k} + \Omega_i^{\text{force},k}\right) \Delta t^k \right) & \cos\left(\left(\omega_i^k + \Omega_i^{\text{torque},k} + \Omega_i^{\text{force},k}\right) \Delta t^k \right) \end{bmatrix} \mathbf{m}_i^k. \tag{A.17}$$

Simulating magnets is the solving of systems of stiff ordinary differential equations (ODEs). At large distances, forces are small, so large timesteps should be used. At short distances, forces are large, so small timesteps should be used. In each iteration of this simulation, the timestep Δt^k was chosen such that the maximum translational movement of the spheres was limited to a maximum 10% of the smallest sphere diameter and the maximum rotational movement of the spheres was limited to $\frac{\pi}{24}$, i.e.,

$$\Delta t^k = \min \left\{ \frac{0.1 \cdot \min_i R_i}{\max_i \left\| \mathbf{v}_i^k + \mathbf{u}_i^{\text{force},k} + \mathbf{u}_i^{\text{torque},k} \right\|}, \frac{\pi}{24} \frac{1}{\max_i \left| \omega_i^k + \Omega_i^{\text{torque},k} + \Omega_i^{\text{force},k} \right|} \right\}. \tag{A.18}$$

27

However, the behavior of the simulation was sometimes unstable, based on the chosen parameters. It is therefore recommended to use the built-in stiff ODE solvers of MATLAB, such as ode23tb. For this, the equations have to be rewritten in the form of a system of ODEs. This was done in later simulations and is explained there.

A 3D version of the spherical dipoles was constructed, before the 2D simulations described above. This simulation was built on the 3D-equivalents of the equations presented above. The two main differences are that it does not include the stiction force, as this was not investigated by then, and the fluid velocity effects were modeled using the Oseen-Burger tensor as described in [3]. This was a less complete fluid flow estimation, as it included only the translational flow resulting from translational movement. It didn't include the translational flow as a result of sphere rotation, nor the vorticity of the fluid flow. Later simulations were done in 2D to reduce computing times.

To analyze the resulting clustering behavior of the spheres, code to detect clusters of spheres was written. Spheres connected within 1.5 times their radius were grouped. A convex hull of the group was calculated, resulting in the approximate area size a and the circumference p of the cluster. The roundness of the clusters was estimated as $4\pi a/p^2$, which is 1 for a circle and goes down to 0 for less circular shapes.

A.2.1 Results

Using the sphere simulation, we can see how magnetic spheres attach and form a straight line (figure A.2A), aligning their magnetic moments. Figure A.2B shows how the average distance between dipoles decreases with exponential 'jumps', explained by the magnetic force which decays with the fourth power of distance. It also shows that the angle between the dipoles goes to 0.

The formed line of magnetic spheres rotates in a rotating magnetic field, but will break apart at higher actuation frequencies (figure A.3). The resulting chain lengths decrease with actuation frequency, which can be explained as follows. The spheres have a maximum achievable translational velocity based on their experienced magnetic and stiction forces. The translational velocity of the spheres increases with actuation frequency and their distance to the center of the chain. As actuation frequency increases, distance to the center of the chain needs to decrease to remain below the maximum translational velocity of the spheres. While no exact relations were investigated, the first patterns emerge: objects group due to their magnetic force, in which the distance between objects is very important. Further, objects have a maximum rotational velocity before they no longer can follow the field. Figure A.4 shows the cluster simulation in 2D, together with the algorithm that can track and analyze the clusters of spheres.
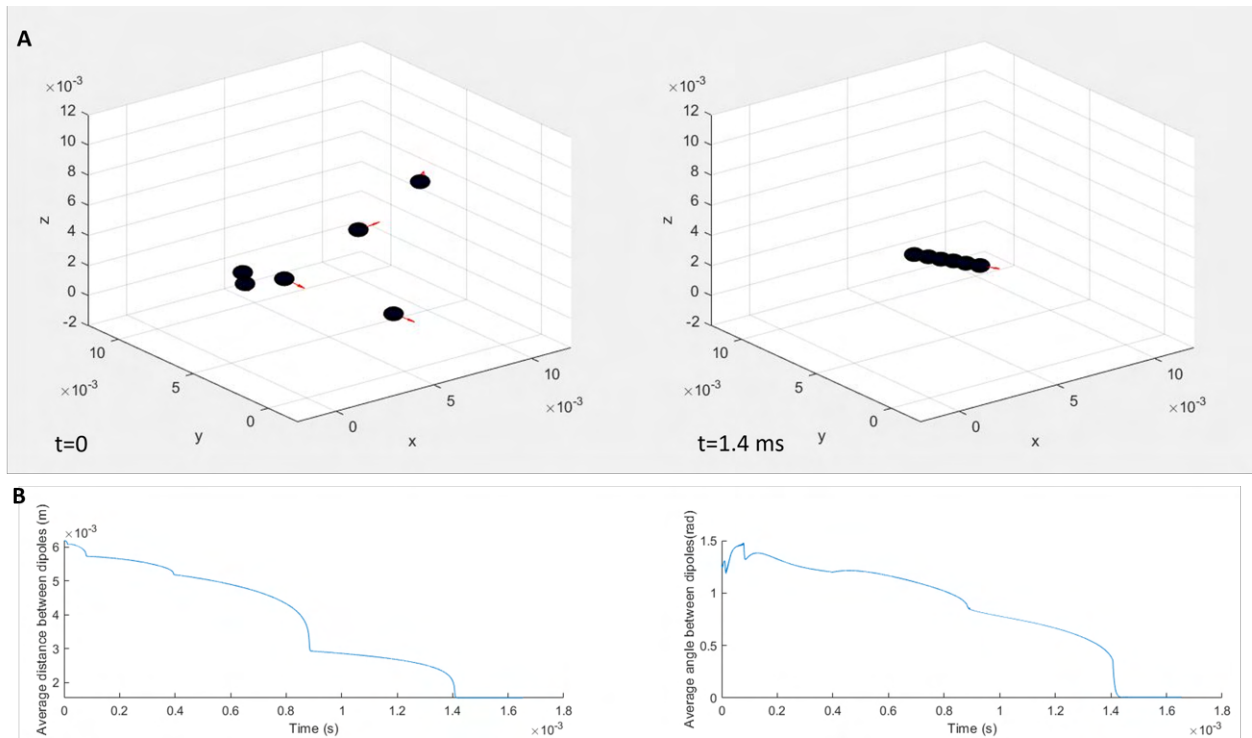
Figure A.2: **(A)** Magnetic spheres are generated in random non-overlapping positions. They quickly attach to form a chain. **(B)** Information about the chain formation process can be extracted. The distance between the spheres decreases and their magnetic moments align.
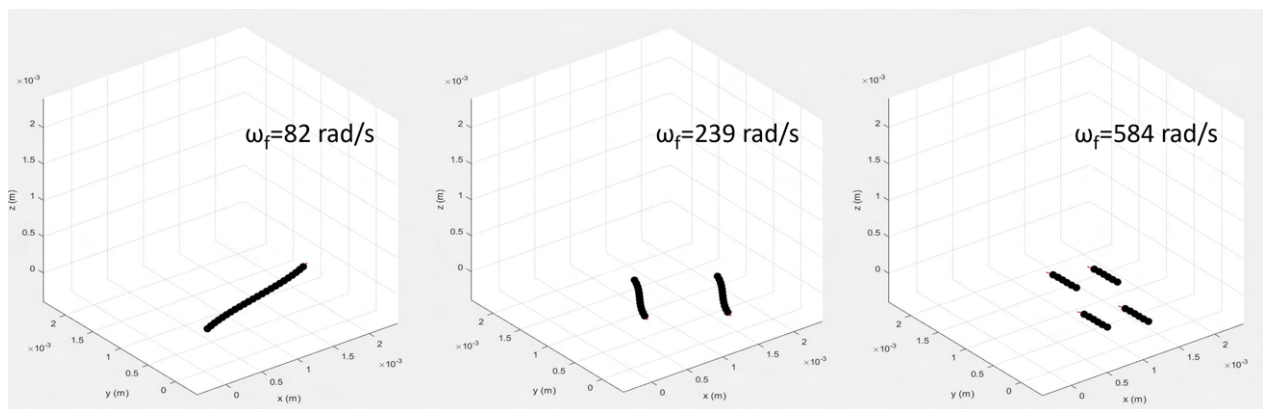

Figure A.3: Actuating a line of magnetic spheres at increasing frequency causes the line to break into smaller and smaller parts.
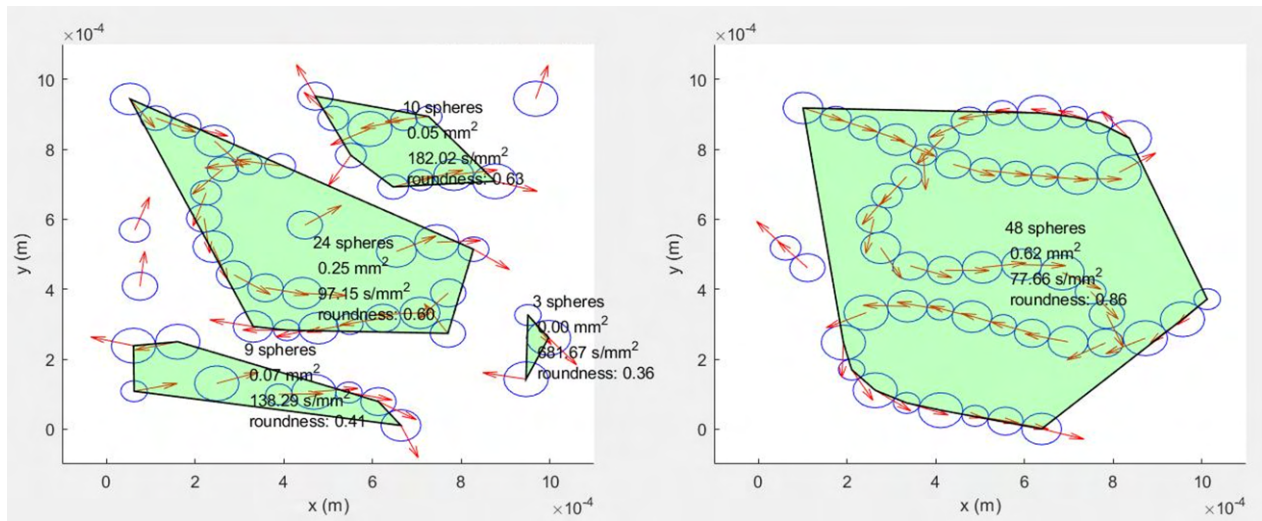
Figure A.4: Cluster tracking in 2D. As the initial idea of the thesis was to also investigate cluster shaping, this was created.
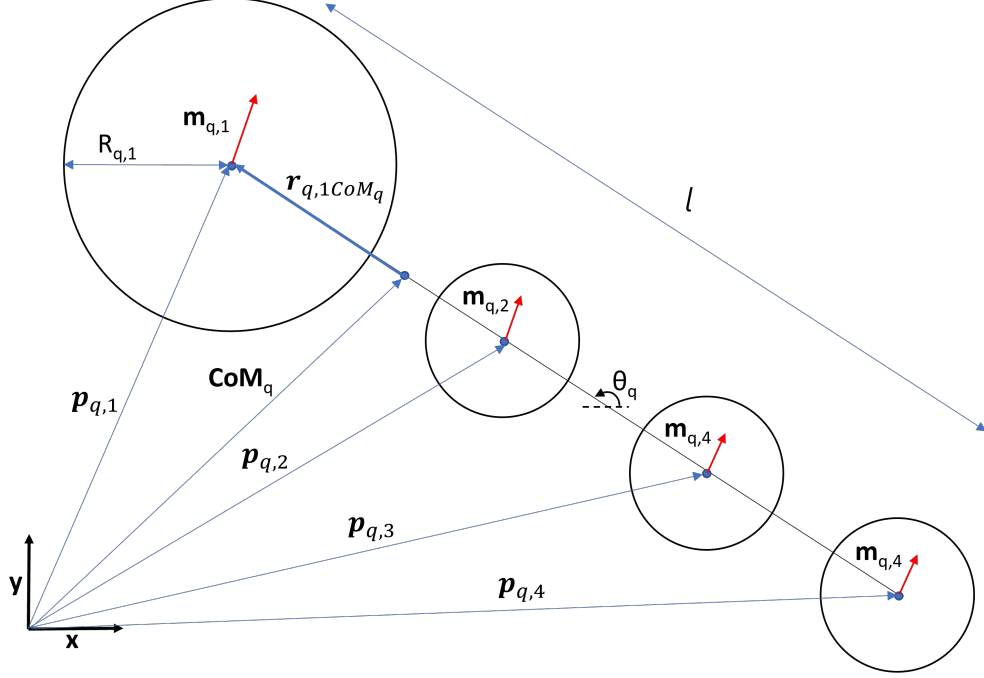
Figure A.5: Representation of the variables used to describe the IRONSperm-like structures in the simulations.

A.3 IRONSperm Clustering

As spheres are not a sufficient representation of the IRONSperm shape, but are computationally efficient, IRONSperm were replicated as rigid, straight chains of paramagnetic spheres. Q IRONSperm were generated, each with a random orientation θ_q (figure A.5). Each IRONSperm consists of H spheres with radius $R_{q,h}$, where the subscript q, h indicates the h'th sphere of IRONSperm q, equally divided over the length l of the IRONSperm. The first sphere has a larger diameter, l_h, than the other spheres, $l_h/8$, to simulate the large head and thin flagellum of sperm cells. Due to the different sphere sizes, the center of mass of these IRONSperm is not in the center of the IRONSperm, but closer to its head. The center of mass of an IRONSperm was chosen as

$$\mathbf{CoM}_q = \frac{\sum_{h=1}^{h=H} V_{q,h} \mathbf{P}_{q,h}}{\sum_{h=1}^{h=H} V_{q,h}}, \tag{A.19}$$

where $V_{q,h}$ is the volume of the sphere at position $\mathbf{p}_{q,h}$. This volume is calculated as $V_{q,h} = \frac{4}{3\pi} \frac{l}{2H} R_{q,h}^2$, to take into account the volume of the rod that is not taken up by the spheres. The IRONSperm are treated as soft magnets. Whilst spheres are used for the physical representation of the IRONSperm, soft-magnetic prolate ellipsoids are used for the magnetic representation. Each sphere is given the magnetic moment of a soft-magnetic ellipsoid as described in [7]. An aspect ratio of $R = l/(H \min_h(R_{q,h}))$ and a magnetic volume of $\frac{4}{3\pi} \frac{l}{2H} (\min_h(R_{q,h}))^2$ is used. The orientation of the long axis of each ellipsoid is the same as θ_q. As the minimum sphere diameter is used to calculate the magnetic volume and aspect ratio for each sphere, each sphere has the same magnetic moment. This was done because in reality, the magnetic moment of a particular part of the IRONSperm is based on the number of nanoparticles, which doesn't necessarily correlate to the size of the respective part.

The movement of the IRONSperm was written as a system of ordinary differential equations:

$$\begin{bmatrix} \dot{\mathbf{p}} \\ \dot{\boldsymbol{\theta}} \\ \omega_{\mathrm{f}} \end{bmatrix} = \begin{bmatrix} \mathbf{F}(t, \mathbf{p}, \boldsymbol{\theta}) \\ \mathbf{G}(t, \mathbf{p}, \boldsymbol{\theta}) \\ 2\pi B_{\mathrm{freq}}, \end{bmatrix}, \tag{A.20}$$

31

where $\dot{\mathbf{p}}$ is the translational velocity of each sphere, $\dot{\boldsymbol{\theta}}$ is the angular velocity of each sphere, and B_{freq} is the frequency of the applied external field. The functions $\mathbf{F}$ and $\mathbf{G}$ are found in a similar way as described in section A.2. However, where the spheres were described as single points, now were dealing with multipoint rigid bodies, which needs to be accounted for. First, the magnetization of each IRONSperm part is calculated as described in [7], using the orientation of the IRONSperm, the external field, and the magnetization parameters. The magnetic forces $\mathbf{F}_{q,h}^{\text{mag}}$ on each magnetic moment of each part of each IRONSperm due to all other magnetic moments are calculated using (A.1). The torques $\tau_{q,h}^{\text{mag}}$ on each magnetic moment due to the external magnetic field and all other magnetic moments are calculated using (A.6) and (A.7). Now that the force and torque on each part of the rigid body is known, these forces and torques need to be converted to movement. Here, the assumption is made that once two IRONSperm touch, they connect and behave together as one rigid body. This was done not only because of the easier programming, but also because the IRONSperm clusters *in vitro* seemed to behave as rigid bodies. Two IRONSperm were considered connected once at least one of the spheres' centers of both IRONSperm were within 1.1 times the sum of the spheres' radii of each other. The algorithm to find which IRONSperm are connected can be found on GitHub. If two or more IRONSperm connect, a new center of mass $\mathbf{CoM}_q$ is calculated, based on the position and volume of each sphere, similar to (A.19). From now on, each group of IRONSperm and individual IRONSperm will be called a cluster, as the following process is the same for both. We reuse the indexing q, h for cluster q, sphere h. The total force on each cluster is

$$\mathbf{F}_q^{\text{tot}} = \mathbf{F}_q^{\text{drag}} + \sum_{h=1}^{H} \mathbf{F}_{q,h}^{\text{mag}} = 0. \tag{A.21}$$

The stiction force and excluded volume force are no longer required, as we've assumed that once spheres touch, they become part of the same rigid body. The drag force $\mathbf{F}_q^{\text{drag}}$ is given by (A.4). The used translational drag coefficient for individual IRONSperm was approximated as that of a prolate ellipsoid with axis of symmetry l and radial axes l_h moving in a random direction, and given by $-3\pi\eta l \ln^{-1}\left(\frac{l}{l_h/2}\right)$ [5]. For multiple connected IRONSperm, the drag coefficient of a prolate ellipsoid with the dimensions of the minimum area enclosing ellipse of the cluster [8] was used.

The total torque on each cluster is given by

$$\tau_q^{\text{tot}} = \tau_q^{\text{drag}} + \sum_{h=1}^{H} \tau_{q,h}^{\text{mag}} + \tau_{q,h}^{\text{F}} = 0, \tag{A.22}$$

where τ_q^{drag} indicates the drag torque the cluster as a whole experiences, given by (A.4). The rotational drag coefficient f_r for individual IRONSperm was approximated as that of a prolate ellipsoid with axis of symmetry l and radial axes l_h, rotating about one of its radial axes, and given by $8\pi\eta(l/2)^3/(3\ln\left(\frac{l}{l_h/2}\right) - 1.5)$. For multipe IRONSperm, again a minimum area enclosing prolate ellipsoid was used to find the drag coefficient. Torque $\tau_{q,h}^{\text{F}}$ is the torque exerted on the cluster by the magnetic forces working on sphere h, given by

$$\tau_{q,h}^{\text{F}} = \mathbf{r}_{q,hCoM_q}^{\perp} \cdot \mathbf{F}_{q,h}^{\text{mag}}, \tag{A.23}$$

where $\mathbf{r}_{q,hCoM_q}^{\perp}$ is the vector perpendicular to the vector from the center of mass of a cluster to the center of sphere h of that cluster, rotated 90° counter-clockwise.

We rewrite (A.21) and (A.22) to find the linear velocity $\mathbf{v}_q$ and the angular velocity ω_q of each cluster, similarly to how this was done in (A.10) and (A.11). The angular velocity of each sphere $\dot{\boldsymbol{\theta}}$ is equal to the angular velocity of the cluster that spheres belongs to, ω_q. The linear velocity of each sphere is given by the sum of the linear velocity of the cluster and the linear velocity caused by the rotation of the cluster,

$$\mathbf{v}_{q,h} = \mathbf{v}_q + \omega_q \begin{bmatrix} \mathbf{CoM}_{q,y} - \mathbf{p}_{q,h,y} \\ \mathbf{p}_{q,h,x} - \mathbf{CoM}_{q,x} \end{bmatrix}, \tag{A.24}$$

where the x and y subscripts indicate the x- and y-components of the vectors, respectively. Only the fluid dynamics are not yet in the model. Now that the translational and rotational velocities of each sphere are known, we transform them to forces and torques using (A.4) and (A.8) with the drag coefficients for each

sphere. We calculate the fluid flow based on these forces and torques using (A.12) to (A.15). The fluid flow at the position of each sphere is transformed back back to forces and torques acting on each sphere using (A.4) and (A.8) with the drag coefficients for each sphere. Finally, we recalculate the (angular) velocity of each sphere in each cluster using the same steps as above. We have found the system of differential equations which we can solve using MATLAB's `ode23tb`. A final feature that was implemented in this simulation is to simulate rolling behavior. For this, a wall location is chosen, e.g., the line y=0. For each cluster, the lowest point below this line is found, and the cluster is rotated about this point instead of its center of mass.

A.3.1   Results

The IRONSperm simulation shows how paramagnetic sperm-like objects cluster in a rotating magnetic field (figure A.6). In this simulation, effects of different field parameters on the clustering time can be found. Figure A.7A shows for that sperm cells initiated at the same position, clustering time decreases quadratically with applied field strength. This is due to the fact that the magnetization of the sperm cells, and therefore the force between the cells, increases quadratically with field strength. Figure A.7B shows clustering time increases with field frequency. This is due to the fact that the phase angle of the clusters increases with field frequency, and therefore magnetization and attractive forces decrease. At 11 Hz, the step-out frequency of the IRONSperm is reached, meaning the sperm cells start oscillating in the field. Clustering time still increases, due to the decreasing magnetization. However, the pattern is seemingly more random, as the magnetic moments of the sperm cells no longer rotate with the field. This changes the attractive forces between the sperm cells.
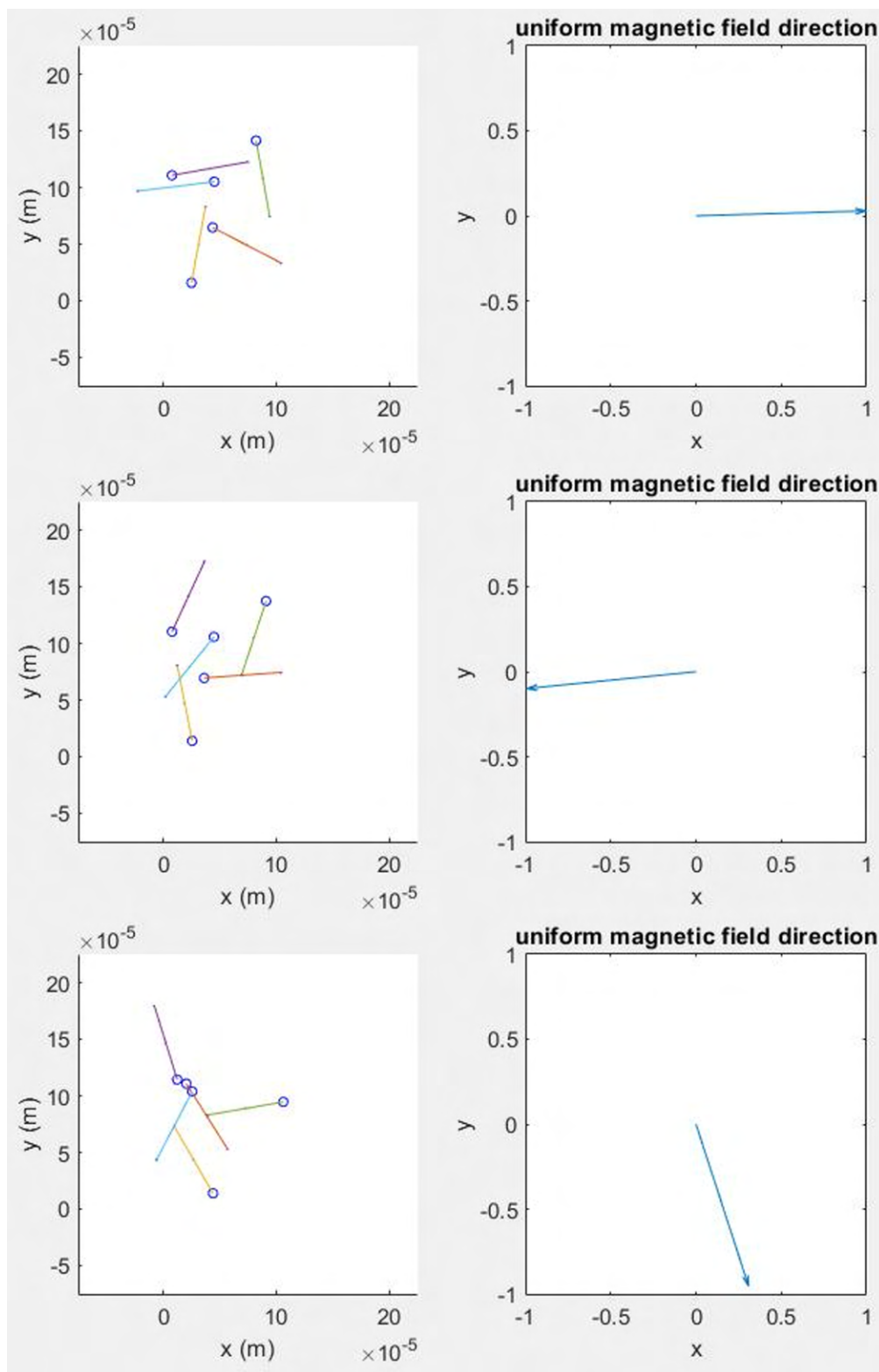
Figure A.6: Each row shows the IRONSperm locations and orientations and field orientation over time (top to bottom). The sperm cells attach and rotate together in the rotating magnetic field.
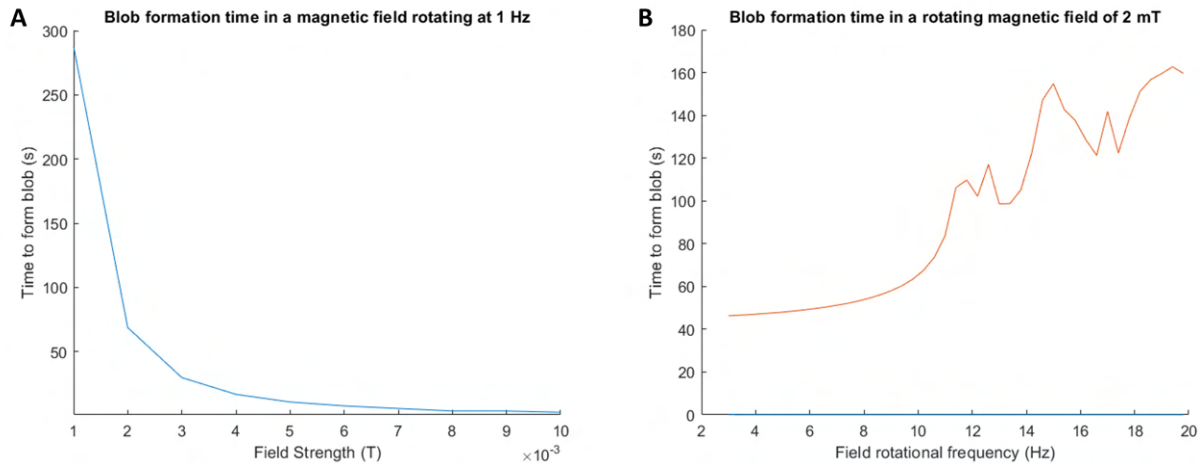
Figure A.7: **(A)** Clustering time decreases quadratically with the field strength, as the magnetization and attractive forces increase. **(B)** Clustering time increases with the field frequency, as the magnetization and attractive forces decrease.

A.4 Stokes Flow

An important part of figuring out how to create IRONSperm clusters, was whether the fluid dynamics were relevant. E.g., larger actuation frequencies would induce stronger flows in the fluid surrounding the clusters. Was this beneficial to cluster formation? A short analysis of (A.12) to (A.15) was done. Previous code of the sphere simulations was used, except all magnetic effects were disabled. Instead, forces and torques were applied manually, to see if the spheres could be brought closer together purely based on the fluid dynamics.

A.4.1 Results

Applying a force to a sphere can be used to bring it closer to another sphere. The other sphere is not pushed further by the fluid than the movement of the other sphere. When a force is applied to a single sphere, it moves slower than when the same force is applied to two neighboring spheres. This is because in the situation of two spheres, the movement of each sphere pushes/pulls the other sphere via the fluid motion [6]. Theoretically, multiple close-by clusters will therefore move faster than a single cluster.

Of course, we cannot apply magnetic forces using a uniform magnetic field. Applying torque to spheres does not bring two spheres closer together (figure A.8). The fluid motion is perpendicular to the radial direction of a sphere. However, the vorticity caused by the rotating sphere can rotate the other sphere.

Introducing a third sphere can bring two spheres closer together. The dynamics when more than two spheres are in near vicinity are chaotic, meaning small changes in initial conditions result in drastically different outcomes [6]. An example of the seemingly random trajectory of a sphere in this environment is shown in figure A.9.

The fluid dynamics do not help when clustering two clusters. In an area where more than two clusters are present, fluid dynamics can help to bring clusters closer together. It was not investigated whether the hydrodynamic benefits of fast rotations outweigh the resulting decreased magnetization and thus the magnetic attractive force.
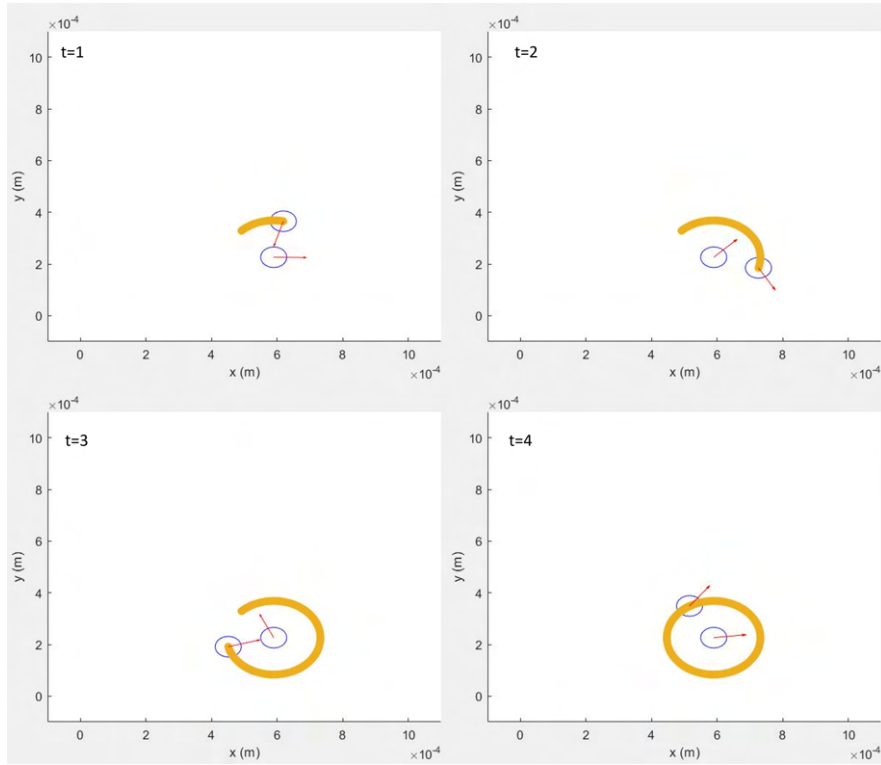
Figure A.8: Applying torque to a sphere does not bring it closer to another sphere by fluid dynamics. The time indications only represent the order of the images.
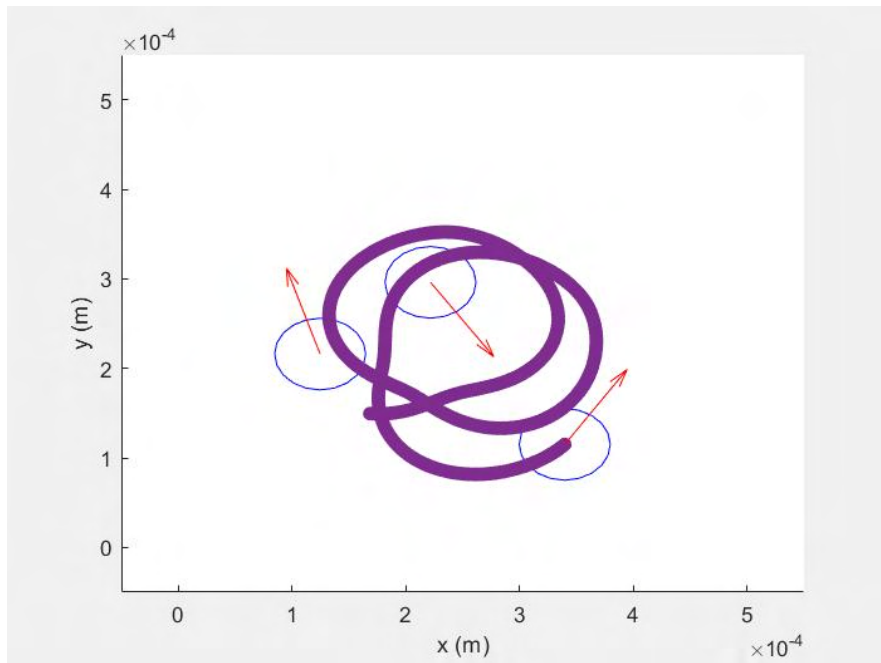

Figure A.9: The purple line shows the seemingly random trajectory of a sphere when torques are applied to all three spheres.

36

A.5 (Para)Magnetic Dipole Movement

In the article, the behavior of soft magnets in a rotating field is summarized as an average attractive force per rotation. However, this doesn't take into account the movement of the dipoles during rotation, which the vector between the dipoles and thus the force between them. In these simulations, a deeper investigation of the movement patterns of dipoles in a low-Reynolds number environment in a rotating field is performed via simulations.

Mathematical Intermezzo

Two spherical dipoles with aligned magnetic moments $\mathbf{m}_1$ and $\mathbf{m}_2$, i.e., the angle between the magnetic moments is zero and the angle between $\mathbf{r}$ and each magnetic moment is also zero, exert a force $\mathbf{F}$ on each other according to (A.1). Filling in the magnetic moments gives
$\mathbf{F}_{12} = -\mathbf{F}_{21} = \frac{3\mu_0}{4\pi \|\mathbf{r}_{12}\|^4} \left(\|\mathbf{m}_2\| \mathbf{m}_1 + \|\mathbf{m}_1\| \mathbf{m}_2 - 4 \|\mathbf{m}_1\| \|\mathbf{m}_2\| \hat{\mathbf{r}}_{12} \right)$. In a low Reynolds environment, the
resulting velocity of each dipole is $\mathbf{v}_i = \frac{\mathbf{F}_{ij}}{f_{t,i}}$ Without loss of generality, let's assume $\hat{\mathbf{r}}_{12} = [-1, 0, 0]^T$.
As we're dealing with a one-dimensional problem now, the distance $r(t)$ between two aligned dipoles starting at position r_0, as a function of time is given by

$$r(t) = r_0 - \int_0^t v_1(t) - v_2(t) dt$$

$$= r_0 - \left(\frac{1}{f_{t,1}} + \frac{1}{f_{t,2}} \right) \int_0^t F_{12}(t) dt$$

$$= r_0 - \frac{3\mu_0}{2\pi} \|\mathbf{m}_1\| \|\mathbf{m}_2\| \left(\frac{1}{f_{t,1}} + \frac{1}{f_{t,2}} \right) \int_0^t r(t)^{-4} dt.$$

This integral equation can be solved analytically. The constant term before the integral will be denoted by a for readability:

$$r(t) = r_0 - a \int_0^t r(t)^{-4} dt,$$

$$\frac{dr(t)}{dt} = \lim_{dt \to 0} \frac{r(t + dt) - r(t)}{dt}$$

$$= \lim_{dt \to 0} \frac{\left(r_0 - a \int_0^{t+dt} r(\tau)^{-4} d\tau \right) - \left(r_0 - a \int_0^t r(\tau)^{-4} d\tau \right)}{dt}$$

$$= -a \lim_{dt \to 0} \frac{\int_t^{t+dt} r(\tau)^{-4} d\tau}{dt}$$

$$\approx -a \lim_{dt \to 0} \frac{r(t + \frac{dt}{2})^{-4} dt}{dt}$$

$$= -ar(t)^{-4}.$$

Solving this differential equation gives the solution

$$r(t) = \sqrt[5]{r_0^5 - \frac{15\mu_0}{2\pi} \|\mathbf{m}_1\| \|\mathbf{m}_2\| \left(\frac{1}{f_{t,1}} + \frac{1}{f_{t,2}} \right) t}, \quad \text{for } 0 \le t \le \frac{2\pi r_0^5}{15\mu_0 \|\mathbf{m}_1\| \|\mathbf{m}_2\| \left(\frac{1}{f_{t,1}} + \frac{1}{f_{t,2}} \right)}.$$

With this solution it is evident that the time to collision ($r(t_{\text{col}}) = 0$) scales with the fifth order of initial distance. The time to collision decreases with the magnetization, and increases with the drag coefficients of the objects. The results of the simulations match this solution.

Two dipoles are initiated at random positions $\mathbf{p}_i$. Their magnetization $\mathbf{m}_i$ rotates with a certain angular velocity ω_f, such that $\mathbf{m}_i = [\cos(\omega_f t) \quad \sin(\omega_f t)]^T$, to mimic that the dipoles follow a rotating uniform magnetic field. The torques between the dipoles are ignored, as they're assumed to be much smaller than the torque exerted by the external field. The force on each dipole due to the other dipole is calculated using (A.1). The force results in a velocity via the drag coefficient of the dipoles, which was set to 1. This results in the following system of differential equations,

$$\begin{bmatrix} \dot{\mathbf{p}}_1 \\ \dot{\mathbf{p}}_2 \end{bmatrix} = \begin{bmatrix} \mathbf{F}_1^{\text{mag}} \\ \mathbf{F}_2^{\text{mag}} \end{bmatrix}, \tag{A.25}$$

which was solved using MATLAB's `ode23tb`.

A.5.1 Results

The approaching paths of dipoles in a rotating field is dependent on the angular velocity of the field (figure A.10A). However, the time to collision is independent of the field frequency. In a DC-field, the approaching path is dependent on the angle between the magnetic moments of the clusters and the vector between the initial positions of the dipole (figure A.10B). The time to collision increases drastically with this angle. To decide whether a DC or rotating field should be used, the times to collision can be compared (figure A.10C). Collision in a rotating field takes 4 times longer than when dipoles are optimally aligned in a DC-field. However, a rotating field is much quicker to collide dipoles than less optimally aligned dipoles in a DC field.

Therefore, in situations where the torque between the dipoles can be ignored, multiple strategies can be used, depending on the wanted outcome. To make two dipoles collide the fastest, align their magnetic moments with the vector between their positions. However, to make randomly oriented dipoles collide, e.g., in a sample with many dipoles, a rotating magnetic field guarantees attractive forces between all dipoles.
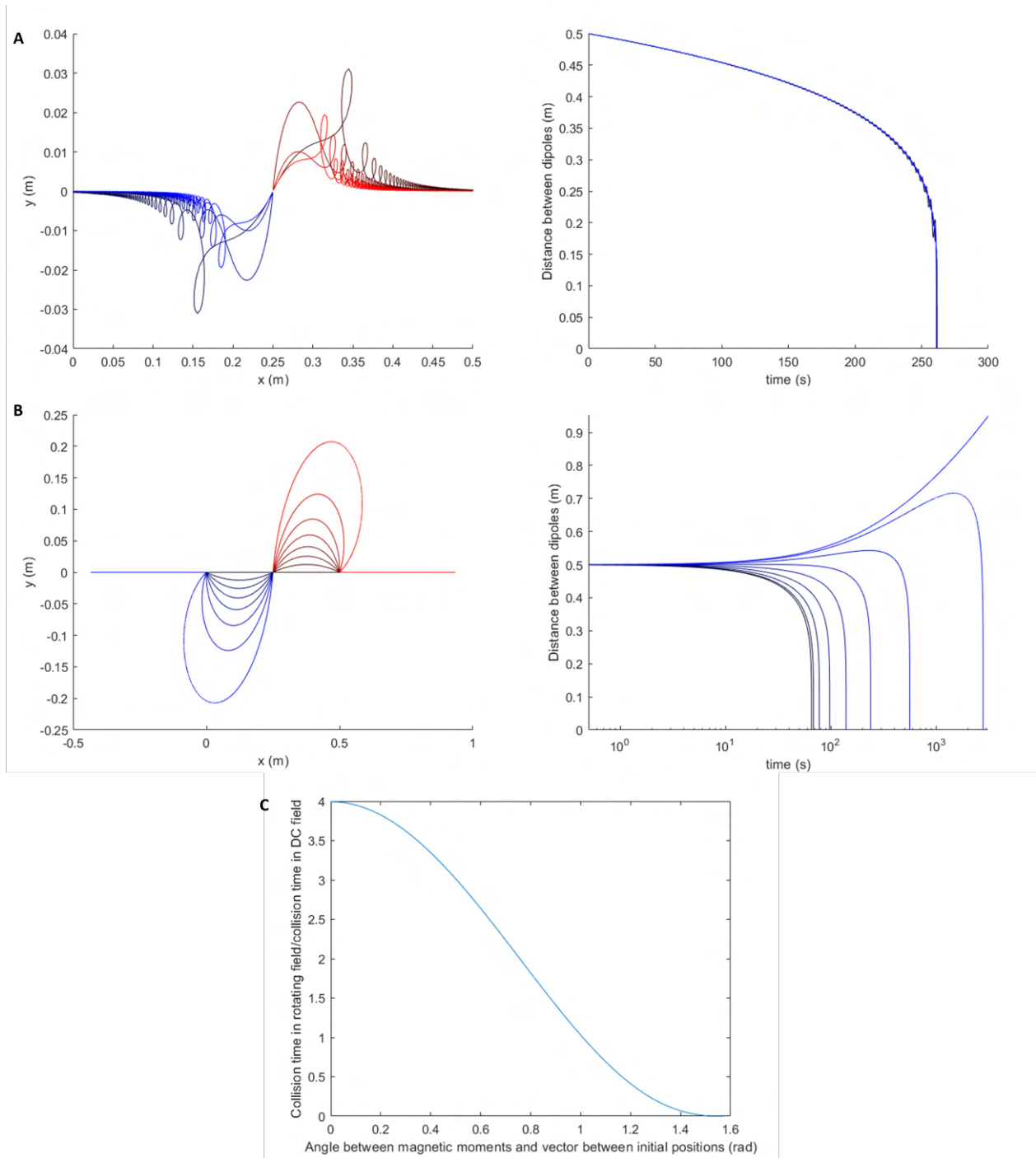
Figure A.10: **(A)** The red and blue lines are the path for each of the dipoles. Lighter colors indicate larger field frequencies. The approaching paths differ for different field frequencies. However, the right graph shows that the total time to collision is approximately constant. **(B)** In a static field, the paths of both dipoles is dependent on the angle between the magnetic moments and the vector between the initial position of the dipoles. Lighter colors indicate a larger angle. The right graph shows collision time is heavily influenced by this angle. **(C)** The time to collision is independent of field frequency in a rotating field, but heavily dependent on the position of the clusters in a DC-field. The rotating field is up to 4 times slower to make dipoles collide, but much faster than the slowest DC-field collision times.

References

[1] Kaz Middelhoek. GitHub Thesis Code, 2021. URL `https://github.com/KazMiddelhoek/Thesis-Code`.

[2] Kar W Yung, B Landecker, and Daniel D Villani. An Analytic Solution for the Force Between Two Magnetic Dipoles. *Magnetic and Electrical Separation*, 9:39–52, 1998.

[3] Yang Gao. *Active mixing and catching using magnetic particles*. PhD thesis, TU Eindhoven, Eindhoven, 10 2013. URL `https://doi.org/10.6100/IR759475`.

[4] J D Jackson. *Classical Electrodynamics*. Wiley, 2 edition, 1975. ISBN 9780471431329.

[5] Howard C. Berg. *Random Walks in Biology*. Princeton University Press, 11 2018. doi: 10.2307/j. ctv7r40w6.

[6] Élisabeth Guazzelli and Jeffrey F. Morris. *A physical introduction to suspension dynamics*. Cambridge University Press, 1 2011. ISBN 9780511894671. doi: 10.1017/CBO9780511894671.

[7] Jake J. Abbott, Olgaç Ergeneman, Michael P. Kummer, Ann M. Hirt, and Bradley J. Nelson. Modeling magnetic torque and force for controlled manipulation of soft-magnetic bodies. *IEEE Transactions on Robotics*, 23(6):1247–1252, 12 2007. ISSN 15523098. doi: 10.1109/TRO.2007.910775.

[8] Nima Moshtagh. Minimum Volume Enclosing Ellipsoids, 2009. URL `https://nl.mathworks.com/matlabcentral/fileexchange/9542-minimum-volume-enclosing-ellipsoid`.

B   Derivations of Equations

B.1   Introduction

This appendix shows the derivations of the equations in the article, and some other derivations that were not included in the article but could prove useful in the future.

B.2   Average Attractive Force Between Rotating Dipoles

A cluster with a magnetic moment $\mathbf{m}_1$ will exert a force on a cluster with a magnetic moment $\mathbf{m}_2$. This force is given by [1]

$$\mathbf{F}_\mathrm{m} = \frac{3\mu_0}{4\pi|\mathbf{r}|^4}\left(\mathbf{m}_2\left(\mathbf{m}_1\cdot\hat{\mathbf{r}}\right) + \mathbf{m}_1\left(\mathbf{m}_2\cdot\hat{\mathbf{r}}\right) + \hat{\mathbf{r}}\left(\mathbf{m}_1\cdot\mathbf{m}_2\right) - 5\hat{\mathbf{r}}\left(\mathbf{m}_1\cdot\hat{\mathbf{r}}\right)\left(\mathbf{m}_2\cdot\hat{\mathbf{r}}\right)\right), \tag{B.1}$$

where $\hat{\mathbf{r}}$ is the unit vector from $\mathbf{m}_1$ to $\mathbf{m}_2$ and $|\mathbf{r}|$ is the distance between the clusters. The force of $\mathbf{m}_2$ on $\mathbf{m}_1$ is opposite in direction. Let us assume $\mathbf{r} = \begin{bmatrix} r & 0 \end{bmatrix}^T$, $\mathbf{m}_1 = |\mathbf{m_1}|\begin{bmatrix} \cos(\varphi) & \sin(\varphi) \end{bmatrix}^T$ and $\mathbf{m}_2 = |\mathbf{m_2}|\begin{bmatrix} \cos(\varphi - \varphi_\mathrm{d}) & \sin(\varphi - \varphi_\mathrm{d}) \end{bmatrix}^T$, where φ is the angle between $\mathbf{r}$ and $\mathbf{m}_1$ and φ_d is the angle between $\mathbf{m}_1$ and $\mathbf{m}_2$. As the clusters align with an external magnetic field, $-\pi/2 \le \varphi_\mathrm{d} \le \frac{\pi}{2}$. Substitution in (B.1) and projection of $\mathbf{F}_\mathrm{m}$ on $-\hat{\mathbf{r}}$ gives

$$\mathbf{F}_\mathrm{m}\cdot(-\hat{\mathbf{r}}) = \frac{3\mu_0|\mathbf{m}_1||\mathbf{m}_2|}{4\pi|r|^4}\left(2\cos(\varphi)\cos(\varphi - \varphi_\mathrm{d}) - \sin(\varphi)\sin(\varphi - \varphi_\mathrm{d})\right), \tag{B.2}$$

which is maximum for $\varphi = \varphi_\mathrm{d} = 0$. The direction of the field relative to $\mathbf{r}$ dictates whether the clusters will attract or repel. In this analysis, the magnetic torque exerted by the clusters is neglected, as it is assumed that the torque of the magnetic field is much larger than the torque of the clusters. In a rotating external field, the average force between two clusters is given by

$$\frac{1}{2\pi}\int_0^{2\pi}\mathbf{F}_\mathrm{m}\cdot(-\hat{\mathbf{r}})d\varphi = \frac{3\mu_0|\mathbf{m}_1||\mathbf{m}_2|}{8\pi|r|^4}\cos(\varphi_\mathrm{d}). \tag{B.3}$$

This analysis shows the average attractive force over one field cycle is one quarter of the maximum attractive force, achieved when aligning $\mathbf{m_1}$ and $\mathbf{m_2}$ with $\mathbf{r}$.

B.3   Rotational Motion of a Cluster in a Rotating Magnetic Field

In a low Reynolds number (low-Re) environment, the rotational motion of a cluster is governed by the torque exerted by viscous drag $\boldsymbol{\tau}_\mathrm{d}$ and the torque exerted by an external magnetic field $\boldsymbol{\tau}_\mathrm{m}$, such that

$$\boldsymbol{\tau}_\mathrm{d} + \boldsymbol{\tau}_\mathrm{m} = 0. \tag{B.4}$$

The torque exerted by viscous drag can be expressed as

$$\boldsymbol{\tau}_\mathrm{d} = -f_\mathrm{r}\boldsymbol{\omega}_\mathrm{c}, \tag{B.5}$$

where $f_{\rm r}$ is the drag coefficient of the cluster and $\omega_{\rm c}$ is its angular velocity. The rotational drag coefficient of a cluster is dependent on the axis of rotation and the dimensions of the cluster. When approximating the cluster with a prolate ellipsoid rotating about its radial axis, the drag coefficient is given by [2]

$$f_{\rm r} = \frac{32}{3} \pi \eta (a^4 - b^4) \left(\frac{2(2a^2 - b^2)}{\sqrt{a^2 - b^2}} \ln \left(\frac{a + \sqrt{a^2 - b^2}}{b} \right) - 2a \right)^{-1}, \tag{B.6}$$

where a is the length of the semi-axis of symmetry of the prolate ellipsoid, b is the length of the radial semi-axis, and η is the viscosity of the surrounding fluid. The torque exerted by an external magnetic field is given by

$$\boldsymbol{\tau}_{\rm m} = \mathbf{m} \times \mathbf{B}, \tag{B.7}$$

where $\mathbf{B}$ is the external magnetic field and $\mathbf{m}$ is the magnetic moment of the cluster.

The cluster can be assumed to be permanently or soft magnetic. If the cluster is permanently magnetic, the cluster has some independent $\mathbf{m}$. If the cluster is soft magnetic, the magnetic moment can be approximated by assuming a soft magnetic ellipsoid of revolution. It is assumed that there is no hysteresis effect, the ellipsoid is not saturated by the external field, the individual domains of the ellipsoid do not interact, and the ellipsoid is relatively small, such that the external field changes linearly along the body [3]. Assuming a large volume magnetic susceptibility, the magnetic moment of a soft-magnetic ellipsoid of revolution $\mathbf{m}$ increases with the external magnetic field $\mathbf{B}$, such that

$$\mathbf{m} = \frac{V}{\mu_0} \begin{bmatrix} \frac{1}{n_a} & 0 & 0 \\ 0 & \frac{1}{n_{\rm r}} & 0 \\ 0 & 0 & \frac{1}{n_{\rm r}} \end{bmatrix} \mathbf{B}, \tag{B.8}$$

where V is the volume of the ellipsoid, μ_0 is the is the vacuum permeability, and n_a and $n_{\rm r}$ are the demagnetizing factors in the axis of symmetry and radial direction of the ellipsoid, respectively. Note that $\mathbf{m}$ and $\mathbf{B}$ are written with respect to the ellipsoid body frame. For a prolate ellipsoid, n_a is given by [3]

$$n_a = \frac{1}{R^2 - 1} \left(\frac{R}{2\sqrt{R^2 - 1}} \ln \left(\frac{R + \sqrt{R^2 - 1}}{R - \sqrt{R^2 - 1}} \right) - 1 \right), \tag{B.9}$$

where $R = a/b > 1$. The demagnetizing factor $n_{\rm r}$ can be found via the relation $n_a + 2n_{\rm r} = 1$.

By applying an external magnetic field in the plane of the axis of symmetry and a radial axis, the problem can be analyzed in two-dimensional space. Let $\mathbf{B}$ be the rotating magnetic field in the global reference frame, given by

$$\mathbf{B} = |\mathbf{B}| \begin{bmatrix} \cos(\theta_{\rm f}(t)) \\ \sin(\theta_{\rm f}(t)) \end{bmatrix} = |\mathbf{B}| \begin{bmatrix} \cos(\omega_{\rm f} t) \\ \sin(\omega_{\rm f} t) \end{bmatrix}, \tag{B.10}$$

where $|\mathbf{B}|$ is the field strength, $\theta_{\rm f}(t)$ is the angle of the magnetic field with the global x-axis at time t, and $\omega_{\rm f}$ is the angular velocity of the rotating magnetic field. Substitution of (B.10) into (B.4) and using either the soft or permanently magnetic assumption results in the following differential equation:

$$\omega_{\rm c} = \frac{d\theta_{\rm c}}{dt} = \begin{cases} \dfrac{|\mathbf{B}|^2 \, |n_a - n_{\rm r}| \, V}{2\mu_0 n_a n_{\rm r} f_{\rm r}} \sin\left(2\left(\omega_{\rm f} t - \theta_{\rm c}\right)\right), & \text{soft magnet,} \\[4mm] \dfrac{|\mathbf{B}||\mathbf{m}|}{f_{\rm r}} \sin(\omega_{\rm f} t - \theta_{\rm c}), & \text{permanent magnet,} \end{cases} \tag{B.11}$$

where $\theta_{\rm c}$ is the angle between the axis of symmetry of the ellipsoid and the global x-axis. This differential equation has two regions of interest, $\omega_{\rm f} \leq \omega_{\rm so}$ and $\omega_{\rm f} > \omega_{\rm so}$, where $\omega_{\rm so}$ is the step-out frequency. The step-out frequency is the maximum angular velocity at which the ellipsoid can rotate in sync with the external field. The step-out frequency is found when (B.11) is maximum, such that [4]

$$\omega_{\rm so} = \begin{cases} \dfrac{|\mathbf{B}|^2 \, |n_a - n_{\rm r}| \, V}{2\mu_0 n_a n_{\rm r} f_{\rm r}}, & \text{soft magnet,} \\[4mm] \dfrac{|\mathbf{B}||\mathbf{m}|}{f_{\rm r}}, & \text{permanent magnet.} \end{cases} \tag{B.12}$$

The step-out frequency of the soft magnet scales with the square of the applied field strength. The step-out frequency of the permanent magnet scales linearly with the field strength. Substitution of the volume and drag coefficient of the ellipsoid in (B.12) and using $R = a/b$ shows that the step-out frequency of a soft-magnetic ellipsoid is independent of the volume of the ellipsoid, and solely dependent on R. For example, when a prolate ellipsoid rotates about one of its radial axes, ω_{so} is given by

$$\frac{\omega_{\mathrm{so}}}{|\mathbf{B}|^2} = \frac{|n_{\mathrm{a}} - n_{\mathrm{r}}|}{16\eta\mu_0 n_{\mathrm{a}} n_{\mathrm{r}}} \frac{(4R^3 - 2R)\ln\left(R + \sqrt{R^2 - 1}\right) - 2R^2\sqrt{R^2 - 1}}{(R^4 - 1)\sqrt{R^2 - 1}}, \tag{B.13}$$

Using the same argument for oblate ellipsoids and rotations about other axes shows volume independence for all combinations of ellipsoid types and rotation axes. The step-out frequency of a prolate ellipsoid rotating about one of its radial axes is maximum for $R \approx 10.31$. An oblate ellipsoid rotating about one of its radial axes has a maximum step-out frequency for $R \approx 10.71$. The step-out frequency during rotation about the axis of symmetry is strictly increasing with R for both kinds of ellipsoids of revolution.

Below the step-out frequency, the angle θ between the external magnetic field and the axis of symmetry of the ellipsoid at any time t, increases with ω_{f} to a maximum at ω_{so} via

$$\theta = \begin{cases} \dfrac{1}{2}\arcsin\left(\dfrac{\omega_{\mathrm{f}}}{\omega_{\mathrm{so}}}\right), & \text{soft magnet,} \\[3mm] \arcsin\left(\dfrac{\omega_{\mathrm{f}}}{\omega_{\mathrm{so}}}\right), & \text{permanent magnet.} \end{cases} \tag{B.14}$$

This angle is found by setting $\omega_{\mathrm{c}} = \omega_{\mathrm{f}}$ in (B.11). Substitution of $\mathbf{B} = \begin{bmatrix} \cos(\theta) & \sin(\theta) & 0 \end{bmatrix}^T$ in (B.8) shows the magnetic moment of a soft-magnetic ellipsoid and θ are inversely proportional, such that

$$|\mathbf{m}| = \frac{V|\mathbf{B}|}{\mu_0 n_{\mathrm{r}} n_{\mathrm{r}}} \left(n_{\mathrm{r}}^2 + \left(-\frac{3}{4}n_{\mathrm{r}}^2 - \frac{1}{2}n_{\mathrm{r}} + \frac{1}{4}\right)\cos^2(\theta)\right)^{\frac{1}{2}}. \tag{B.15}$$

Therefore, combined with (B.14) we find the magnetic moment of a soft-magnetic ellipsoid decreases with ω_{f}. High field strength and low field frequency maximizes the magnetic moment of soft-magnetic clusters.

Above the step-out frequency, the ellipsoid starts to oscillate. This oscillation pattern is found in the solution to (B.11). For the soft magnetic case, this solution is

$$\theta_{\mathrm{c}}(t) = \theta_{\mathrm{f},0} + \omega_{\mathrm{f}}t - \arctan\left(\tan\left((\omega_{\mathrm{f}}t - C)\sqrt{1 - \left(\frac{\omega_{\mathrm{so}}}{\omega_{\mathrm{f}}}\right)^2}\right)\sqrt{1 - \left(\frac{\omega_{\mathrm{so}}}{\omega_{\mathrm{f}}}\right)^2} + \frac{\omega_{\mathrm{so}}}{\omega_{\mathrm{f}}}\right), \tag{B.16}$$

where $\theta_{\mathrm{f},0}$ is the orientation of the magnetic field at $t = 0$, and C is dependent on the angle of the ellipsoid at $t = 0$, $\theta_{\mathrm{c},0}$, such that

$$C = \frac{\arctan\left(\dfrac{\tan(\theta_{\mathrm{c},0} - \theta_{\mathrm{f},0}) + \frac{\omega_{\mathrm{so}}}{\omega_{\mathrm{f}}}}{\sqrt{1 - \left(\frac{\omega_{\mathrm{so}}}{\omega_{\mathrm{f}}}\right)^2}}\right)}{\sqrt{1 - \left(\frac{\omega_{\mathrm{so}}}{\omega_{\mathrm{f}}}\right)^2}}. \tag{B.17}$$

This solution is found by first substituting $u = \omega_{\mathrm{f}}t - \theta_{\mathrm{c}}$, performing a Weierstrass substitution, and completing the square. For the permanent magnet case, the amplitude of the oscillations is doubled and the frequency halved, i.e., a factor two is added before the arctan and a factor $1/2$ is added before t. Due to the discontinuity in the tangent function, (B.16) needs to be 'phase unwrapped' to accurately represent the physical rotation, i.e., as the oscillation passes $-\frac{\pi}{2}$, the next angle should not be interpreted as $\frac{\pi}{2}$, but as $\frac{\pi}{2} - \pi$.

With the solution to the differential equation, parameters that characterize the rotational motion of the ellipsoid can be derived. For example, the average angular velocity of the ellipsoid is given by

$$\omega_{\mathrm{c}} = \frac{1}{T}(\theta_{\mathrm{c}}(t + T) - \theta_{\mathrm{c}}(t)) = \omega_{\mathrm{f}} - \omega_{\mathrm{f}}\sqrt{1 - \left(\frac{\omega_{\mathrm{so}}}{\omega_{\mathrm{f}}}\right)^2}, \tag{B.18}$$

where T is the period of the oscillation, $\pi / \left(\omega_\mathrm{f} \sqrt{1 - \left(\frac{\omega_\mathrm{so}}{\omega_\mathrm{f}} \right)^2} \right)$ for the soft magnet. Both the soft and permanent magnets result in the same average angular velocity.

Of course, with the period of the oscillations now known, other parameters can be derived, such as the number of oscillations per field rotation n, the oscillation frequency divided by the field frequency, given by

$$
n = \begin{cases}
2\sqrt{1 - \left(\dfrac{\omega_\mathrm{so}}{\omega_\mathrm{f}} \right)^2}, & \text{soft magnet,} \\[4mm]
\sqrt{1 - \left(\dfrac{\omega_\mathrm{so}}{\omega_\mathrm{f}} \right)^2}, & \text{permanent magnet.}
\end{cases}
\tag{B.19}
$$

The number of oscillations per field rotation increases with ω_f to a maximum of 2 for soft magnets and to 1 for permanent magnets. Similar parameters may prove useful in the future to estimate step-out frequencies.

A final parameter is the apparent oscillation amplitude θ_osc, the angle between the moment the ellipsoid stops following the field and the moment the ellipsoid starts following the field again, for soft magnets given by

$$
\theta_\mathrm{osc} = \theta_\mathrm{c}(t_{\pi/2}) - \theta_\mathrm{c}(t_0) = \frac{\pi}{2} - \left(\frac{\pi}{2} + \arctan\left(\frac{-\omega_\mathrm{so}}{\omega_\mathrm{f}\sqrt{1 - \left(\frac{\omega_\mathrm{so}}{\omega_\mathrm{f}} \right)^2}} \right) \right) \left(1 - \left(\frac{\omega_\mathrm{so}}{\omega_\mathrm{f}} \right)^2 \right)^{-\frac{1}{2}},
\tag{B.20}
$$

where t_0 is the time where the oscillation changes sign from positive to negative (the ellipsoid start lagging behind) and $t_{\pi/2}$ is the time where the oscillation changes sign from negative to positive (the ellipsoid starts catching up). Equation (B.20) shows that θ_osc decreases as ω_f increases.

References

[1] Kar W Yung, B Landecker, and Daniel D Villani. An Analytic Solution for the Force Between Two Magnetic Dipoles. *Magnetic and Electrical Separation*, 9:39–52, 1998.

[2] Francis Perrin. Mouvement brownien d'un ellipsoide-I. Dispersion diélectrique pour des molécules ellipsoidales. *J. Phys. Radium*, 5(10):pp, 1934. doi: 10.1051/jphysrad:01934005010049700{\"{i}}. URL `http://dx.doi.org/10.1051/jphysrad:01934005010049700`.

[3] Jake J. Abbott, Olgaç Ergeneman, Michael P. Kummer, Ann M. Hirt, and Bradley J. Nelson. Modeling magnetic torque and force for controlled manipulation of soft-magnetic bodies. *IEEE Transactions on Robotics*, 23(6):1247–1252, 12 2007. ISSN 15523098. doi: 10.1109/TRO.2007.910775.

[4] Arthur W. Mahoney, Nathan D. Nelson, Kathrin E. Peyer, Bradley J. Nelson, and Jake J. Abbott. Behavior of rotating magnetic microrobots above the step-out frequency with application to control of multi-microrobot systems. *Applied Physics Letters*, 104(14):144101, 4 2014. ISSN 00036951. doi: 10.1063/1.4870768. URL `https://aip.scitation.org/doi/abs/10.1063/1.4870768`.